UNIVERSITAT POLITÈCNICA DE CATALUNYA
BARCELONATECH
Escola Superior d'Enginyeries Industrial,
Aeroespacial i Audiovisual de Terrassa

Study on secondary flow losses modellig in compressor cascades using Reynolds Averaged Navier-Stokes techniques

BACHELOR FINAL THESIS

Document:

Report

Author:

Zobaer Ahmed Salam

Director/Co-director:

Jordi Ventosa Molina

Degree:

Bachelor in Aerospace Vehicle Engineering

Examination session:

Spring 2023

Acknowledgements

I would like to express my sincere gratitude to Jordi Ventosa Molina, the project director, for his guidance, expertise, and trust in me throughout this research endeavour. His mentorship and insightful advice have been fundamental in shaping this thesis.

Furthermore, I extend my heartfelt appreciation to my parents for their unwavering support. Their constant encouragement and belief in my abilities have been a constant source of inspiration and motivation throughout my academic journey. Their sacrifices and guidance have played an integral role in my personal and academic growth.

Finally, I want to express appreciation to all the professors who have taught and mentored me during my degree. Their knowledge, dedication, and passion for their respective fields have had a profound impact on my academic development. Their guidance and support in and outside the classroom have been fundamental in shaping my academic journey and fostering a love for learning.

To all those mentioned above, and to anyone who has contributed to my academic and personal growth, I am deeply grateful for your invaluable support and guidance.

Abstract

The present study explores the feasibility of using the GEKO turbulence model in Ansys Fluent software to analyze secondary flow losses in turbomachinery compressors. This turbulence model includes free parameters that can be adjusted to enhance simulation accuracy. The model was calibrated to match reference data obtained from a Large Eddy Simulation (LES), by focusing on two dimensional simulations at the midspan of the compressor blade. Subsequently, the obtained calibrated values were used to perform three dimensional simulations. The calibrated GEKO model showed similar results to the default GEKO model, indicating limited improvement. However, both GEKO models outperformed the standard $k-\omega$ model in predicting pressure losses. Vortical structures, such as the tip leakage vortex, were captured by all simulations. The positioning of the vortex in the GEKO simulations was consistent with the reference data. However, the $k-\omega$ model showed displacements with respect to the LES simulation. These findings highlight the potential of the GEKO model for practical applications in turbomachinery compressor analysis.

Declaration of Honour

I, Zobaer Ahmed Salam, solemnly declare that I am the author of this final thesis entitled Study on secondary flow losses modellig in compressor cascades using Reynolds Averaged Navier-Stokes techniques. I have undertaken this research work independently and without unauthorized assistance or plagiarism.

I affirm that all the information, data, and materials used in this thesis are acknowledged and appropriately cited, giving credit to the original authors and sources. I have made every effort to ensure that all the sources consulted and referenced are accurately cited in the bibliography, following the required academic citation style.

Furthermore, I acknowledge that any direct quotations, paraphrases, or borrowed information from other works are clearly identified and attributed to their respective authors. I have diligently followed the ethical guidelines and academic integrity standards in the production of this thesis.

I take full responsibility for the originality and authenticity of this work, ensuring that it represents my own contributions. I understand that any breach of academic integrity or misrepresentation may have serious consequences, including the rejection of this thesis and the potential disciplinary actions by the UPC-ESEIAAT.

I hereby affirm that this declaration is made in good faith, with honesty, and in accordance with the principles of academic integrity.

Zobaer Ahmed Salam,

21/06/2023

Contents

List of Figures

List of Tables

Chapter 1

Introduction

1.1 Background and Motivation

Over the past few decades, there has been an emphasis on enhancing the overall efficiency and reducing the core engine dimensions in the development of flight propulsion gas turbines. Enhanced efficiency is achieved by increasing compression ratios, resulting in greater pressure gradients between the pressure and suction sides of gas turbine blades. This increase of the pressure gradient magnifies the flow passing through the casing gap, which contributes in increasing the effects of secondary flows. Moreover, the downsizing of the engine contributes to an augmented area-to-volume ratio, which substantially amplifies the impact of the endwall. The latter is the main cause of increased secondary flow effects in this study case.

In fluid dynamics, primary flow refers to the dominant flow pattern in a fluid system. It represents the primary motion of the fluid, and is typically driven by external forces or boundary conditions. On the other hand, secondary flows are understood as deviations from the primary flow. As aforementioned, in this study case, these additional flow patterns are primarily caused by the casing gap and the endwall effects. The created vortices due to the secondary flow induce instabilities, and the flow field becomes three-dimensional and hard to predict. Secondary flows have a very high impact in efficiency, accounting for up to 30% [1] of the losses in compressors and turbines in turbo-machines. The correct description of the vortex structures is essential to design more efficient gas turbines, which will contribute to reduce CO_2 emissions and fuelling costs.

The flow inside a compressor is axisymmetric, and three main zones can be identified at each blade: root, mid-span, and tip. The flow at the mid-span has been historically studied using algebraic expressions, but secondary flows have a stronger presence in the root and tip sections, making them harder to model. One of the main secondary flow structures is the tip leakage vortex (TLV). The latter arise from the flow that passes through the necessary gap between blades and sidewalls, this gap allows the rotation of the machine. This flow feature is one of the main sources of inefficiencies. Hence, understanding and also predicting it is key when designing new blades for turbomachinery.

In the recent years, the tendency is to recur to computational fluid dynamics (CFD) techniques in order to describe secondary flows. Depending on the level of modelling, three different frameworks can be defined: Direct Numerical Simulations (DNS), Large Eddy Simulations (LES), and Reynolds Averaged Navier Stokes equations simulations (RANS). No modelling is used in DNS simulations, the Navier-Stokes equations are solved directly by using numerical methods. This method provides the most accurate results, but it requires a substantial amount of computing power, due to the high density meshes employed to solve all the energy scales of the flow (energy scales are described in the following chapter). In LES simulations, large energy scales are solved directly and small scales are filtered out and modelled. LES simulations still need relatively high computing power. At last, RANS simulations time-average the Navier-Stokes equations, and model all the scales. They require coarser meshes than the previous methods, therefore, requiring less computational power. This is the least expensive solution, however, uncertainty is introduced due to the assumptions made while modelling the equations.

New RANS turbulence models, such as the GEKO model, have shown noticeable improvements describing complex flows. This model provides free parameters that can be adjusted according to the study case. This project will tackle the description of secondary flows using a calibrated GEKO model. This will help to understand the underlying physics of secondary flow vortices. The main requirement of the project will be verifying the results with high fidelity simulations data.

1.2 Requirements

- **Ansys Software:** The simulations will be carried out with the Ansys's simulation software. This package also includes CAD and meshing tools, which will also be used for the geometry definition and meshing processes. The Student version of the software will be used.
- **Mesh Elements Limitations:** The Student version of the Ansys software has a maximum number of mesh elements. On the other hand, the simulations will be performed on a computer using an *Intel i5-6600* processor and 16 GB of RAM. The mesh convergence study will be performed according to the software and hardware limitations.
- **Assessment of the Results:** Simulation results will be compared against high fidelity LES simulations. The assessment of the results will involve commonly studied parameters in flows through compressors, i.e. total pressure losses at the row outlet, pressure and friction coefficients at the blade surface. Furthermore, large vortical structures will also be assessed.
- **GEKO Model:** The RANS model to be used will be the Generalised $k-\omega$.
- **Final Report:** At the end of the project, a final report containing the results and their discussion will be produced.

1.3 Scope

- **Literature Review:** In order to understand the study case, a literature review of fluid dynamics, turbulence models, and basis of computational fluid dynamics (CFD) will be required.
- **Geometry and Boundary Conditions Definition:** The blade's geometry will me drawn using computer assisted drawing (CAD) programs, and a 3D model will be created. The boundaries will be described to characterize the case. This includes specifying the wall types (stationary or moving), their roughness, symmetry conditions and periodic conditions.
- **Meshing:** The fluid domain will be discretized using finite volumes. The mesh will be refined near the critical zones.
- **Convergence Study:** The obtained results must not depend on the mesh, therefore, different meshes will be created, increasing their density at each iteration, until the results converge.
- **Free GEKO Parameters Calibration:** Once the configuration of the case is established, the free parameters of the GEKO model will be tweaked until the results obtained match with the LES simulations ones.
- **Physical Understanding:** After verifying the obtained results, they will be analysed to understand the physics behind the secondary flow vortices.

1.4 Schedule

The project's planning and timeline are presented in table 1.1 and figure 1.1, respectively. Table 1 provides a comprehensive overview of the project's key activities, milestones, and their respective time-frames. It offers a structured representation of the project's schedule, allowing for a clear understanding of the planned tasks and their sequencing. On the other hand, Figure 1 visually illustrates the project timeline, depicting the duration of each phase or stage, along with task dependencies.

ID	Name	Start Date	End Date	Duration
1	Literature Review	ene 30, 2023	mar 31, 2023	45 days
1.1	Fluid Dynamics Fundamentals	ene 30, 2023	feb 07, 2023	7 days
1.2	RANS eq, Derivation and Different Models	feb 07, 2023	feb 16, 2023	8 days
1.3	Meshing and Wall Treatment	feb 16, 2023	mar 01, 2023	10 days
1.4	Discretization and Numerical Methods	feb 27, 2023	mar 08, 2023	8 days
1.5	Turbomachinery	mar 08, 2023	mar 31, 2023	18 days
2	Basic Simulations	feb 10, 2023	mar 22, 2023	29 days
2.1	Driven Cavity, Channel Flow, and Cylinder	feb 10, 2023	feb 17, 2023	6 days
2.2	2D Channel Flow with Periodic Condition	feb 17, 2023	mar 09, 2023	15 days
2.3	3D Channel Flow with Double Periodicity	mar 02, 2023	mar 22, 2023	15 days
3	Study Case	mar 23, 2023	may 30, 2023	49 days
3.1	CAD Model and Boundary Definition	mar 23, 2023	abr 05, 2023	10 days
3.2	Initial Meshing	abr 05, 2023	abr 13, 2023	7 days
3.3	Mesh Convergence Study	abr 14, 2023	may 11, 2023	20 days
3.4	GEKO Parameters Calibration	may 12, 2023	may 30, 2023	13 days
4	Analysis and Report	may 22, 2023	jun 19, 2023	21 days
4.1	Final Report Redaction	may 22, 2023	jun 19, 2023	21 days

Table 1.1: Schedule

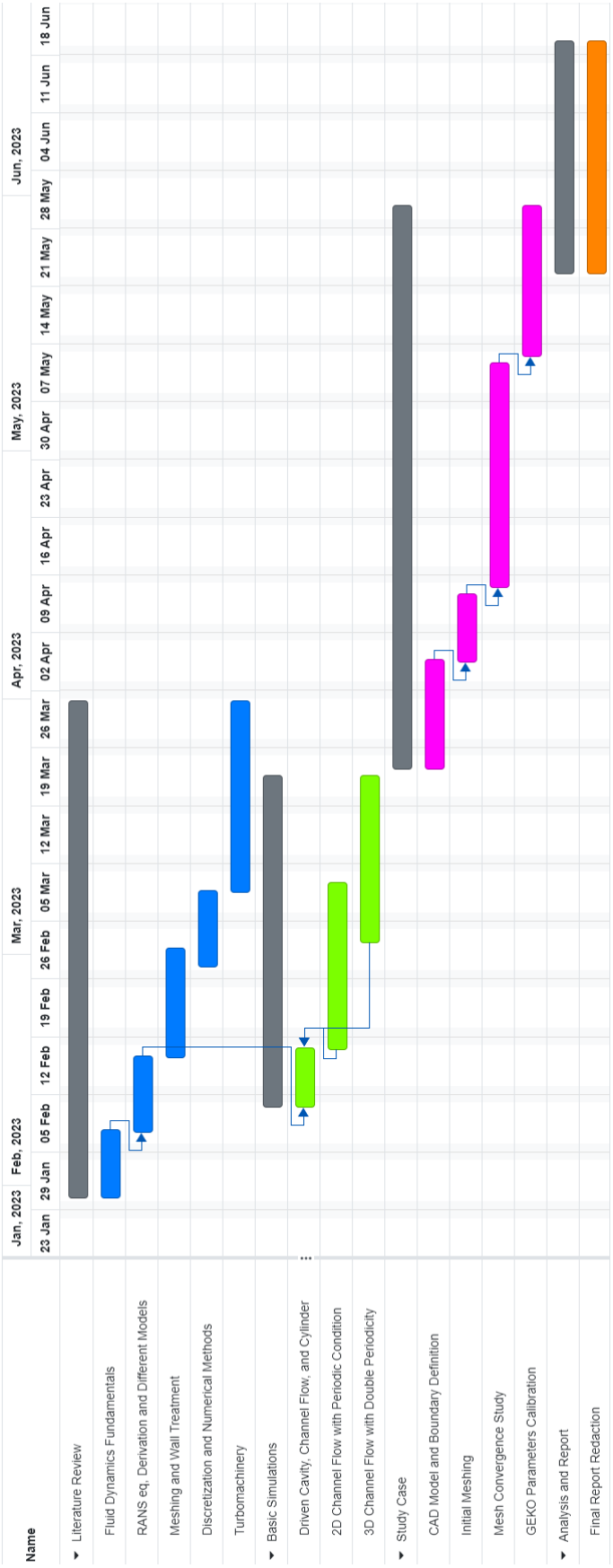

Figure 1.1: Gantt Diagram

Chapter 2

Theoretical Background

2.1 Fundamentals of Fluid Dynamics

2.1.1 Reynolds Transport Equation and Material Derivative

Fluids can be analysed from two points of view, Lagrangian and Eulerian. In the Lagrangian point of view, each particle is followed through time and space. This approach tracks the trajectory of individual particles and examines the change in their properties along their path. This method is useful for particle simulations. On the other hand, the Eulerian approach fixes points in space and analyses how fluid properties change over time at that fixed point. The latter allows the discretization of the fluid domain into a computational grid or mesh.

The governing equations can be converted from one perspective to another by employing the Reynolds transport theorem (eqn 2.1) and the material derivative (eqn 2.2):

$$\left[\frac{dB}{\partial t}\right]_{system} = \int_{CV} \frac{\partial}{\partial t}(b\rho)d\forall + \int_{CS} b\rho\vec{V}\cdot\hat{n}\,dA \tag{2.1}$$

$$\frac{Db}{Dt} = \frac{\partial b}{\partial t} + (\vec{V}\cdot\vec{\nabla})b \tag{2.2}$$

Where B is an extensive property and b an specific property (B/m). The $\forall$ symbol will be employed to represent Volume in order to distinguish it from Velocity.

2.1.2 Conservation Laws

Mass

The mass conservation law states that the net mass flow rate entering or leaving a control volume, is equal to the rate of change of mass within it. Using the mass as the extensive property and plugging it to equation 2.1, the mass conservation or continuity equation is obtained:

$$0 = \int_{CV} \frac{\partial}{\partial t} \rho d\forall + \int_{CS} \rho \vec{V} \cdot \hat{n} \, dA \tag{2.3}$$

Using the divergence theorem, the surface integral can be converted to a volume integral:

$$0 = \int_{CV} \left[\frac{\partial \rho}{\partial t} + \vec{\nabla} \cdot (\rho \vec{V}) \right] d\forall \tag{2.4}$$

Since the latter equation must be equal to zero regardless of the control volume, the continuity equation can be expressed as follows:

$$\boxed{\frac{\partial \rho}{\partial t} + \vec{\nabla} \cdot (\rho \vec{V}) = 0} \tag{2.5}$$

And for an incompressible flow, the following expression is obtained:

$$\boxed{\vec{\nabla} \cdot \vec{V} = 0} \tag{2.6}$$

Momentum

The momentum equation is derived from Newton's Second Law. It establishes a relationship between the forces acting on a fluid element and its acceleration or rate of change of momentum. In this case, momentum $(m\vec{V})$ is the quantity to be transported, therefore, the left side of the transport equation will have force units:

$$\sum \vec{F} = \int_{CV} \frac{\partial}{\partial t} (\rho \vec{V}) d\forall + \int_{CS} (\rho \vec{V}) \vec{V} \cdot \hat{n} \, dA \tag{2.7}$$

The sum of forces can be separated between volume and surface forces:

$$\int_{CV} \rho \vec{g} dV + \int_{CS} \sigma_{ij} \cdot \hat{n} dA = \int_{CV} \frac{\partial}{\partial t} (\rho \vec{V}) d\forall + \int_{CS} (\rho \vec{V}) \vec{V} \cdot \hat{n} \, dA \tag{2.8}$$

Pressure and friction forces are included inside the σ_{ij} stress tensor:

$$\sigma_{ij} = \begin{pmatrix} -p + \tau_{xx} & \tau_{yx} & \tau_{zx} \\ \tau_{xy} & -p + \tau_{yy} & \tau_{zy} \\ \tau_{xz} & \tau_{yz} & -p + \tau_{zz} \end{pmatrix} \tag{2.9}$$

Now applying the divergence theorem on both sides to the surface integrals, the following is obtained:

$$\int_{CV} \left[\frac{\partial}{\partial t} (\rho \vec{V}) + \vec{\nabla} \cdot (\rho \vec{V} \vec{V}) - \rho \vec{g} - \vec{\nabla} \cdot \sigma_{ij} \right] d\forall = 0 \tag{2.10}$$

As in the continuity equation, the equation must be equal to zero regardless of the control volume, therefore:

$$\frac{\partial}{\partial t}(\rho\vec{V}) + \vec{\nabla}\cdot(\rho\vec{V}\vec{V}) = \rho\vec{g} + \vec{\nabla}\cdot\sigma_{ij} \tag{2.11}$$

Now, applying the product rule to the first term of the left side of the previous equation, the following is obtained:

$$\rho\left[\frac{\partial\vec{V}}{\partial t} + (\vec{V}\cdot\vec{\nabla})\vec{V}\right] = \rho\vec{g} + \vec{\nabla}\cdot\sigma_{ij} \tag{2.12}$$

See that the terms inside the brackets are actually the material derivative of V:

$$\boxed{\rho\frac{DV}{Dt} = \rho\vec{g} + \vec{\nabla}\cdot\sigma_{ij}} \tag{2.13}$$

2.1.3 Differential Form of Continuity and Navier-Stokes equations

Further developing the continuity equation for incompressible flows, and the momentum equation in all three directions, one can get a set of equations that descrive incompressible fluid behaviour.

For the continuity equation, the nabla operator is aplied to the velocity field:

$$\boxed{\frac{\partial u}{\partial x} + \frac{\partial v}{\partial y} + \frac{\partial w}{\partial z} = 0} \tag{2.14}$$

Before developing the momentum equation, the σ_{ij} stress tensor elements will be defined. For a Newtonian fluid, the shear stresses can be related to the pressure and velocity field. This relationship is known as the constitutive equation:

$$\tau_{ij} = 2\mu\epsilon_{ij} \tag{2.15}$$

Where μ is the dynamic viscosity. Developing ϵ_{ij}, and substituting the corresponding τ_{ij} components,

$$\sigma_{ij} = \begin{pmatrix} -p + 2\mu\frac{\partial u}{\partial x} & \mu\left(\frac{\partial u}{\partial y} + \frac{\partial v}{\partial x}\right) & \mu\left(\frac{\partial u}{\partial z} + \frac{\partial w}{\partial x}\right) \\ \mu\left(\frac{\partial v}{\partial x} + \frac{\partial u}{\partial y}\right) & -p + 2\mu\frac{\partial v}{\partial y} & \mu\left(\frac{\partial v}{\partial z} + \frac{\partial w}{\partial y}\right) \\ \mu\left(\frac{\partial w}{\partial x} + \frac{\partial u}{\partial z}\right) & \mu\left(\frac{\partial w}{\partial y} + \frac{\partial v}{\partial z}\right) & -p + 2\mu\frac{\partial w}{\partial z} \end{pmatrix} \tag{2.16}$$

Taking equation 2.13 for the x component, and applying the nabla operator to the stress tensor:

$$\rho\frac{Du}{Dt} = -\frac{\partial p}{\partial x} + 2\mu\frac{\partial^2 u}{\partial^2 x} + \mu\frac{\partial}{\partial y}\left(\frac{\partial v}{\partial x} + \frac{\partial u}{\partial y}\right) + \mu\frac{\partial}{\partial z}\left(\frac{\partial w}{\partial x} + \frac{\partial u}{\partial z}\right) + \rho g_x \tag{2.17}$$

Following the same procedure for the other two components, and rearranging the terms by developing the material derivative, the three Navier-Stokes equations are obtained:

$$\rho\left(\frac{\partial u}{\partial t}+u\frac{\partial u}{\partial x}+v\frac{\partial u}{\partial y}+w\frac{\partial u}{\partial z}\right)=-\frac{\partial p}{\partial x}+\mu\left(\frac{\partial^2 u}{\partial x^2}+\frac{\partial u^2}{\partial y^2}+\frac{\partial^2 u}{\partial z^2}\right)+\rho g_x \tag{2.18a}$$

$$\rho\left(\frac{\partial v}{\partial t}+u\frac{\partial v}{\partial x}+v\frac{\partial v}{\partial y}+w\frac{\partial v}{\partial z}\right)=-\frac{\partial p}{\partial y}+\mu\left(\frac{\partial^2 v}{\partial x^2}+\frac{\partial^2 v}{\partial y^2}+\frac{\partial^2 v}{\partial z^2}\right)+\rho g_y \tag{2.18b}$$

$$\rho\left(\frac{\partial w}{\partial t}+u\frac{\partial w}{\partial x}+v\frac{\partial w}{\partial y}+w\frac{\partial w}{\partial z}\right)=-\frac{\partial p}{\partial z}+\mu\left(\frac{\partial^2 w}{\partial x^2}+\frac{\partial w^2}{\partial y^2}+\frac{\partial^2 w}{\partial z^2}\right)+\rho g_z \tag{2.18c}$$

These three equations can also be presented in a compact vectorial form:

$$\rho\frac{DV}{Dt}=-\vec{\nabla}P+\mu\nabla^2\vec{V}+\rho\vec{g} \tag{2.19}$$

The system of equations is now solvable, since there are now four unknown variables; the pressure and three components of velocity, as well as four equations, the Navier-Stokes equations in three components, and the continuity equation.

2.2 Turbulence and CFD Frameworks

2.2.1 Turbulence Introduction

Turbulence is a complex and chaotic phenomenon that occurs in fluid flows, characterized by irregular fluctuations in velocity, pressure and other flow properties. The governing equations presented in the previous chapter contain partial differential equations, which are difficult to solve analytically. This phenomenon's non linear nature is what makes it mathematically complex to study. The understanding of turbulence plays a crucial role in the design of industrial machinery. By comprehending this phenomenon, engineers can accurately predict and optimize fluid behaviour, leading to improved designs, enhaced performance and increased efficiency of engineering systems.

In a fluid flow, energy is transferred across a wide range of length scales, leading to the existence of energy cascades [2, 3, 4]. This concept lies on the idea that there are a wide range of eddies or vortices, each characterized by a size or spatial scale. Each eddy possesses a specific amount of kinetic energy associated with its size. These eddies interact with each other, and the flow's energy is transferred from the larger scales to the smaller ones.

The energy cascade can be split into three conceptually different regions [5]: the integral range, the inertial range, and the dissipation range:

The integral scale region corresponds to the largest eddy of the flow, which is also the the most energy containing one. This scale is defined as the characteristic length scale where energy is distributed in a way that represents the overall flow behaviour. The sizes of its eddies are determined by the size of the energy source or the physical dimensions of the system.

Intermediate size eddies exist within the inertial range. Here, the kinetic energy from large turbulent eddies is transferred to the small eddies. This energy transfer is related to the process of vortex stretching. Vortex stretching occurs when differential rotation rates cause the large scales to elongate and stretch, reducing their radius. Stretching increases the vorticity or the rotation rates of the fluid elements. This process leads to the generation of smaller scales.

As the energy cascade continues into smaller scales, it eventually reaches the dissipation scale. This is the smallest scale in a flow, also known as the Kolmogorov scale. Here the kinetic energy is converted into heat through the action of molecular viscosity [2, 4]. Although the different regions have discussed individually, it is important to note that the energy transfer is continuous.

2.2.2 Direct Numerical Simulation

Direct Numerical Simulation, or DNS is a computational modeling approach that solves the discretized governing equations directly, without any simplification or approximation. This method numerically solves all the flow scales, therefore, it is the most accurate. DNS provides detailed information about the flow field at every point in space and time, and allows a comprehensive understanding of the underlying physics behind the fluid.

This method has a major drawback: it is computationally expensive. This is due to the vast range of scales inherent in turbulent flows. The solution of all flow scales requires using very fine grids and small time scales, this way the motion of the smallest eddies of the flow can be captured. Moreover, the computational cost also grows rapidly with the Reynolds number, since the range of scales in the flow increases with it. The following expression shows the relation between the characteristic length of the flow (L) and the dissipation length scales (η) [4].

$$\frac{L}{\eta} \propto \left(Re^{3/4}\right) \tag{2.20}$$

The previous equation shows how the difference between the smallest and largest length scales increases exponentially. Practical engineering applications often involve high Reynolds number flows, making DNS a non-viable option. Due to its high computational cost, DNS is typically limited to academic research. Simple flow cases can provide detailed insights into turbulence phenomena, which are useful to create new turbulence models.

2.2.3 Large Eddy Simulation

Large Eddy Simulation, or LES is an intermediate computational technique between DNS and RANS. Large scale structures, which contribute significantly to the overall flow behaviour, are solved directly using the governing equations. On the other hand, small scale structures, known as subgrid scales (SGS), are modelled [6, 7]. The Kolmogorov's local isotropy hypothesis states that small scales are statistically isotropic, therefore, they are less affected by the boundary conditions [8, 2]. According to this hypothesis, the behaviour of the smaller scales can be considered universal, and statistical models can be developed. On the other hand, larger scales depend on each study case, resulting in a greater complexity when formulating a general model.

In order to separate the resolved and unresolved scales, a spatial and temporal filtering process is applied to the governing equations. This filtering operation introduces a cutoff scale, which determines the boundary between resolved and modelled scales. Due to the advances in computational power, this method gaining popularity in industrial applications.

2.2.4 Reynolds Averaged Navier Stokes

Reynolds Averaged Navier Stokes, or RANS equations are a widely used modelling approach. This method models all flow scales, enabling the use of coarser grids. Therefore, this model is the least computationally expensive. However, due to the modelling of all flow scales, this method is also often found to present the largest differences compared to experiments. The RANS equations are derived by averaging the fluid governing equations over time, resulting in a time-averaged representation of the flow [9]. Although this model does not provide detailed information of the flow as the previous two methods, the simplified description of the mean flow behaviour is sufficient for many applications in engineering fields.

The velocity in a turbulent flow can be decomposed into a mean and fluctuating part:

$$u = \overline{u} + u' \tag{2.21}$$

Introducing this expression into the governing equations and manipulating them, the continuity and time averaged Navier-Stokes equations are obtained:

$$\boxed{\frac{\partial \bar{u}_i}{\partial x_i} = 0} \tag{2.22}$$

$$\boxed{\rho \bar{u}_j \frac{\partial \bar{u}_i}{\partial x_j} = \rho \bar{f}_i + \frac{\partial}{\partial x_j}\left[-\bar{p}\delta_{ij} + \mu\left(\frac{\partial \bar{u}_i}{\partial x_j} + \frac{\partial \bar{u}_j}{\partial x_i}\right) - \rho\overline{u_i' u_j'}\right]} \tag{2.23}$$

The $\rho\overline{u_i' u_j'}$ in equation 2.23 is called the Reynolds Stress tensor,

$$\rho\overline{u_i' u_j'} = \begin{pmatrix} \overline{u'u'} & \overline{u'v'} & \overline{u'w'} \\ \overline{v'u'} & \overline{v'v'} & \overline{v'w'} \\ \overline{w'u'} & \overline{w'v'} & \overline{w'w'} \end{pmatrix} \tag{2.24}$$

The fluctuating velocities of the Reynolds Stresses are responsible for fluctuations in momentum transfer across different direction. These are unknown variables, therefore, a closure problem arises. These terms are not directly solved by the RANS equations themselves. Closure models are required to completely close the system of equations [9]. The correlations between fluctuating velocities depend on the intricate dynamics of turbulence. The main inconvenience is that these correlations can vary significantly in different flow conditions and geometries. There are a numerous closure models, each demonstrating different degrees of effectiveness on different types of flows. The next sections will provide brief explanations of some of the most commonly employed models.

2.3 RANS Modelling

2.3.1 Dimensionless Distance

Throughout the study, the dimensionless distance y^+ will be mentioned. In fluid dynamics, the y^+ value represents the dimensionless distance of a grid point from a solid boundary. The y^+ value is crucial in determining the appropriate turbulence model and grid resolution for accurate near-wall flow predictions. Generally, for wall-bounded flows, a y^+ value of around 1 is desired to ensure accurate solving of the boundary layer. This typically involves ensuring that the first grid point adjacent to the wall falls within the range of y^+ values close to unity. It is defined as follows:

$$y^+ = \frac{u_\tau y}{\nu} \tag{2.25}$$

where y is the distance from the wall, ν, is the kinematic viscosity of the fluid, and u_τ is the friction velocity, which is defined as follows:

$$u_\tau = \sqrt{\frac{\tau_w}{\rho}} \tag{2.26}$$

being ρ the density, and τ the wall shear stress, which can be determined through empirical correlations, or can be obtained from simulation results.

2.3.2 Boussinesq's Hypothesis and Algebraic Models

The most common approach for modelling the Reynolds stress tensor is recurring to the Boussinesq's eddy viscosity hypothesis [10]. Kolmogorov presented the idea of the energy spectrum [2], where energy is transported in the medium and large scales, and energy dissipation is produced in the small scales. Under this hypothesis, the turbulent fluctuations of the smaller scales are modelled by a diffusive model. This way, the turbulent fluctuations are presented as the product of a turbulent viscosity and the velocity gradient. This hypothesis relates the Reynolds stresses to the mean velocity gradient as described in the following equation:

$$-\rho\overline{u_i' u_j'} = \mu_t \left(\frac{\partial U_i}{\partial x_j} + \frac{\partial U_j}{\partial x_i} - \frac{2}{3}\frac{\partial U_k}{\partial x_k}\delta_{ij} \right) - \frac{2}{3}\rho k \delta_{ij} \tag{2.27}$$

Where δ_{ij} is the delta of Kronecker operator, which takes a value of 1 if $i = j$ and 0 if $i \neq j$. The μ_t term on the other hand, is the turbulent eddy viscosity. The first turbulence models proposed using a fixed mixing length approach to calculate the eddy viscosity. The mixing length l_m represents an indicative size of the turbulent eddies present in the flow. The relationship between the turbulent eddy viscosity and the mixing length can be expressed as [4]:

$$\mu_t = \rho l_m^2 \left| \frac{\partial U}{\partial y} \right| \tag{2.28}$$

There are many approaches to calculate the mixing length, two commonly employed models are the Prandtl approach (equation 2.29) and Van Driest approach (equation 2.30).

$$l_m = \kappa y \quad \text{where} \quad \kappa = 0.41 \tag{2.29}$$

$$l_m = \kappa \left[1 - \exp - \frac{y^+}{A^+} \right] \quad \text{where} \quad A^+ = 26 \tag{2.30}$$

For the boundary layer, in these models, the mixing length is evaluated algebraically at each position of the domain. Consequently, for a given geometry, the mixing lengths and turbulent eddy viscosity will be fixed for each point throughout the entire domain. This approach can provide relatively accurate results for simple two dimensional flows, but for complex geometries it is hard to estimate functions that relate the mixing length to the position. This is a limitation, since turbulence is not static and fixed at a specified distance from the wall. Turbulence is convected and diffuses through the flow. For this reason, a more precise representation of turbulence can be achieved by solving transport equations for the turbulent properties. Detailed explanation of the mixing length models can be found in [3].

2.3.3 $k - \epsilon$ Model

The $k - \epsilon$ model is a widely used approach in RANS simulations. Unlike the algebraic models that rely on fixed values for the mixing length, the $k - \epsilon$ model solves transport equations for the turbulent kinetic energy k and the turbulent dissipation rate ϵ. The turbulent kinetic energy represents the energy associated with the chaotic fluctuations of velocity. The turbulent dissipation rate is the rate turbulent kinetic energy is converted into thermal energy by viscous effects. By solving the transport equations of these quantities, the convective and diffusive behaviour of turbulence can be represented more accurately. Once k and ϵ have been evaluated from their respective transport equations, the turbulent mixing length can be evaluated as:

$$l_m = \frac{C_\mu k^{3/2}}{\epsilon} \tag{2.31}$$

And the turbulent eddy viscosity can be expressed as:

$$\mu_t = C_\mu \frac{\rho k^2}{\epsilon} \tag{2.32}$$

The k quantity is obtained by using the transport equation 2.33 and the ϵ quantity is obtained by using the transport equation 2.34.

$$\frac{D}{Dt}(\rho k) = \nabla \cdot \left[\left(\mu + \frac{\mu_t}{\sigma_k} \right) \nabla k \right] + P_k + P_b - \rho\epsilon \tag{2.33}$$

$$\frac{D}{Dt}(\rho \epsilon) = \nabla \cdot \left[\left(\mu + \frac{\mu_t}{\sigma_\epsilon} \right) \nabla \epsilon \right] + C_1 \frac{\epsilon}{k}(P_k + C_3 P_b) - C_2 \rho \frac{\epsilon^2}{k} \tag{2.34}$$

The P_k term is the production due to mean velocity shear, P_b is the production due to buoyancy. The coefficients C_1, C_2, C_3, σ_k and σ_e are empirical constants. The change of these coefficients can notoriously change the intrinsic physics of turbulence, hence they are only modified in academic research. For general use cases, the latest standard values provided by Launder and Sharma in [11] are used:

$$C_\mu = 0.09 \; C_1 = 1.44, \; C_2 = 1.92, \; C_3 = 0, \; \sigma_k = 1, \; \sigma_\epsilon = 1.3$$

The detailed derivation of this model's equations can be found in [12], and further explanation about the model can be found in the original paper from Jones and Launder in [13].

Even though the $k - \epsilon$ model is a very efficient approach to solve turbulent flows, it has a series of limitations. This model struggles to accurately solve near-wall regions. For low y^+ values ($y^+ < 5$), damping functions are often used. These functions are derived from assumptions that may not be accurate in complex geometry. It is also not adequate for complex flows with presence of strong curvatures and adverse pressure gradients. Swirling flows and recirculation zones are not handled accurately. Due to the mentioned limitations, this model is generally not suitable for external aerodynamics and turbomachinery simulations.

2.3.4 $k - \omega$ Model

The $k - \omega$ model is a two equation model that aims to improve the predictions made when simulating boundary layer behaviour with adverse pressure gradients. This is one of the preferred models for external aerodynamics and turbomachinery simulations. Different versions of this model have been proposed over time. These variations provide different coefficient's calibrations. The transported turbulent quantities in this model are the turbulent kinetic energy k and specific turbulence dissipation rate ω. The later is defined as:

$$\omega = \frac{\epsilon}{C_\mu k} \tag{2.35}$$

Both ϵ and ω represent the same physical magnitude: dissipation of turbulent energy. Using the relationship in equation 2.35, the turbulence dissipation rate can be converted to specific turbulence dissipation rate, and vice versa. The transport equation of the turbulent kinetic energy remains the same as in the $k - \epsilon$ model, with an additional coefficient see equation 2.36. The transport equation for ω is shown in equation 2.37.

$$\frac{D}{Dt}(\rho k) = \nabla \cdot \left[\left(\mu + \frac{\mu_t}{\sigma_k} \right) \nabla k \right] + P_k + P_b - \beta^* \rho \omega k \tag{2.36}$$

$$\frac{D}{Dt}(\rho\omega) = \nabla \cdot \left[\left(\mu + \frac{\mu_t}{\sigma_\omega}\right)\nabla\omega\right] + P_\omega - \beta\rho\omega^2 \tag{2.37}$$

Where P_ω is a production term, given as:

$$P_\omega = \frac{\alpha_\omega \omega}{k} P_k \tag{2.38}$$

The coefficients α_ω, β, β^*, σ_k, σ_ω in the preceding equations need to be set beforehand, based either on experimental or high-fidelity numerical data. These constants can vary between the $k-\omega$ model variations. For the Wilcox (2006) [14] model:

$$\alpha_\omega = \tfrac{13}{25},\ \beta = \tfrac{3}{40},\ \beta^* = \tfrac{9}{100},\ \sigma_k = 0.5,\ \sigma_\omega = 0.5$$

For detailed derivation of the $k-\omega$ model formulation see [15] and [12].

It was mentioned in the previous section that the $k-\epsilon$ model employed damping functions for near-wall regions. The $k-\omega$ model does not use them, therefore, it can resolve boundary layers with adverse pressure gradients more accurately. For this reason, it is preferred in external aerodynamics and turbomachinery applications. The main weakness of this model is its strong dependency on freestream turbulence conditions [16, 17]. Small changes in the inlet turbulent conditions lead to large changes in the turbulent viscosity μ_t. Consequently, this leads to considerable changes in the skin friction coefficient, which is a critical coefficient that will be discussed in the next chapter. To address this limitation, the present study will perform a calibration of the inlet turbulence boundary conditions, considering that the employed model is a variation of the $k-\omega$ model.

2.3.5 Generalized $k-\omega$ Model

Both two equation models presented until this point have model coefficients. These constants are fixed and predetermined by the model itself. They are typically determined through extensive research and calibration processes to ensure their accuracy and reliability. These coefficients are not meant to be modified by normal users, as doing so can have significant implications on the underlying physics of turbulence. The generalized $k-\omega$ or GEKO model is a variation of the standard $k-\omega$ model that provides adjustable free parameters. These parameters can be modified by the user for specific applications without negatively affecting the basic configuration of the model. However, they also have to be modified carefully. For this, Ansys provides best practice guidelines [18].

The GEKO model offers six free parameters: two of them are designed to address wall-bounded flows (CSEP and CNW), two are dedicated to calibrating free shear flows (CMIX and CJET), one is to enhance the prediction of corner flow separation (CCORNER), and finally one is intended for making curvature corrections (CCURV). All these parameters are implemented through functions inside the k and ω transport equations. The exact formulation of these functions has not been provided by Ansys, therefore, it cannot be presented in this report.

- **CSEP:** This is the main parameter for adjusting separation prediction for boundary layers. The impact of this parameter extends to all types of flows. By increasing its value, the eddy viscosity is reduced.

This leads to more sensitivity to adverse pressure gradients within boundary layers, and lower spreading rates for free shear flows.

- **CNW:** This parameter primarily influences the inner region of wall boundary layers. It has limited to no impact on free shear flows. An increase in this parameter results in higher wall shear stress and wall heat transfer rates in non-equilibrium flows. Its effects on non-generic flows, such as vortices, has not been systematically tested yet.
- **CMIX:** This parameter exclusively impacts free shear flows. Its increase leads to higher spreading rates of free shear flows. This coefficient also plays a key-role in compensating the effects of the lowered spreading rates for free shear flows induced by the CSEP parameter. For each value of CSEP an optimal value of CMIX exists. By default, this parameter is automatically calculated using the following correlation: $C_{MIX} = 0.35(C_{SEP} - 1)\sqrt{(|C_{SEP} - 1|)}$.
- **CJET:** This parameter is active in a sub-model of CMIX, and has no impact when CMIX is set to 0. It primarily influences jet flows, its increase results in a decrease in spreading rates of jet flows. It allows to adjust the spreading rate of jet flows while maintaining the spreading rate of the mixing layer.
- **CCORNER:** This parameter introduces a non-linear stress-strain term to account for secondary flows in corners.
- **CCURV:** This parameter corrects flow curvature.

By default, this values are adjusted to mimic the behaviour of the $k - \omega$ SST model, which is a variation of the standard $k - \omega$ model. The default values are the following:

$$C_{SEP} = 1.75,\ C_{NW} = 0.5,\ C_{MIX} = 0.5,\ C_{JET} = 0.9,\ C_{CORNER} = 1,\ C_{CURV} = 1$$

2.4 Turbomachinery Funtamentals

2.4.1 Turbines and Compressors

This section will provide a fundamental overview of turbines and compressors, focusing on the thermodynamic transformations that take place in the flow during the work addition and extraction processes. This description will focus on axial compressors and turbines, since they are the case of study.

Both compressors and turbines consist of multiple stages, typically with compressors having tens of stages and turbines having fewer than ten stages. Each stage is composed of two rows of blades, which are aerodynamically shaped bluff bodies. One row of blades remains fixed and is called stator, while the other one rotates along the axial axis and is referred to as rotor.

In turbines, the stator is positioned ahead of the rotor. The stator's primary function is to convert pressure energy into kinetic energy by properly directing the flow. Subsequently, the rotor extracts kinetic energy from the flow and converts it into mechanical work. In contrast, in compressors, the rotor is placed before the stator. The rotor applies work to the flow increasing its kinetic energy by accelerating it. Then the stator converts that kinetic energy to pressure by redirecting the flow.

To study the flow, two reference frames are set: an absolute reference frame is fixed to the stator, absolute speeds and angles are referenced to this frame; and a relative reference frame is placed and attached to the rotor, relative speeds and angles are referenced to this frame. The latter is a mobile frame which rotates with the same speed as the rotor. A velocity triangle can be drawn with the different velocities and flow angles entering and leaving the rotor. See figure 2.1

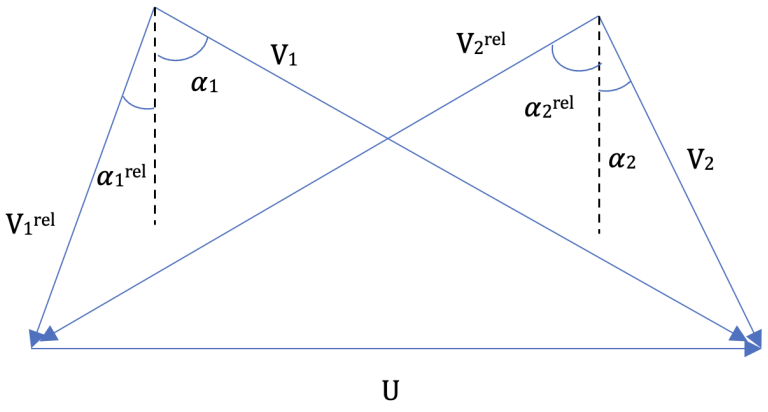

Figure 2.1: Velocity Triangle

The V_1, V_2, α_1 and α_2 will be used to represent velocities and angles in the absolute reference frame. While V_1^{rel}, V_2^{rel}, α_1^{rel} and α_2^{rel} will be used for the relative frame. The "1" subscript refers to flow entering the rotor, and "2" exiting it. In velocity triangles, the maximum velocities are usually found on the left side. Therefore, for a flow in a turbine, where the maximum velocities are found at the rotor entry, the "1" variables would be place at the left and "2" variables would be placed on the right. Conversely, in compressors where the maximum velocities are found at the rotor exit, the placement is reversed, with the "1" variables on the right side and the "2" variables on the left side.

It has to be noted that the analysis of the flow in this section will be performed at the mean radius $r_m = 1/2(r_t + r_h)$, where r_t and r_h represent the tip and hub radius. At each stage, the circumferential speed will be defined as $U = \omega r_m$, where ω represents the rotational speed. Axial and tangential velocities can be obtained as follows:

$$V_a = V \cos \alpha \tag{2.39a}$$

$$V_\theta = V \sin \alpha \tag{2.39b}$$

$$V_\theta = U + V_\theta^{rel} \tag{2.39c}$$

2.4.2 Euler Equation

The power generated by turbomachinery can be analyzed from both mechanical and thermodynamic perspectives. By applying the kinetic moment conservation law to a control volume that surrounds the rotor, the following expression is obtained:

$$M_z = \dot{m}(r_2 V_{\theta,2} - r_1 V_{\theta,1}) \tag{2.40}$$

Then the power developed is expressed as:

$$\dot{W} = M_z \cdot \omega = \omega \dot{m}(r_2 V_{\theta,2} - r_1 V_{\theta,1}) \tag{2.41}$$

Since the analysis is being performed at the mean radius, the work expression becomes:

$$\dot{W} = \dot{m} U (V_{\theta,2} - V_{\theta,1}) \tag{2.42}$$

Power can be related to an stagnation enthalpy change:

$$\dot{W} = \dot{m} \Delta h_0 \tag{2.43}$$

Now equating the mechanical and thermodynamic expressions:

$$\Delta h_0 = U(V_{\theta,2} - V_{\theta,1}) \tag{2.44}$$

Using the vector decomposition shown in equation 2.39, the Euler equation can be obtained in terms of relative velocities or relative angles:

$$\frac{\dot{W}}{\dot{m}} = \Delta h_0 = U(V_{\theta,2} - V_{\theta,1}) = U(V_{\theta,2}^{rel} - V_{\theta,1}^{rel}) \tag{2.45a}$$

$$\frac{\dot{W}}{\dot{m}} = \Delta h_0 = UV_a(\tan\alpha_2 - \tan\alpha_1) = UV_a(\tan\alpha_2^{rel} - \tan\alpha_1^{rel}) \tag{2.45b}$$

From the previous expressions, it is evident that enthalpy variations are caused by tangential velocity changes. In the case of turbines, energy is extracted from the flow by decreasing its angular momentum. On the other hand, in compressors, work introduced by the rotor increases the flow's angular momentum. The axial velocity is not taken into account since the turbomachinery under study rotates around the axial axis and does not exert any work in that direction.

From this analysis, it can be concluded that work can be achieved through high rotational speeds U, high axial velocity V_a, and high fluid deflection in the rotor $\alpha_2^{rel} - \alpha_1^{rel}$. This analysis serves to justify the positioning of the rotor and stator within compressors and turbines. In compressors, the rotor is placed first, where work is applied. This leads to an increase of the flow's kinetic energy by raising its tangential speed. Subsequently, the flow passes through the stator, where no work is applied. Since energy must be conserved, both static pressure and static temperature inrease. In turbines, static enthalpy is converted into kinetic energy in the stator. The flow experiences a pressure and temperature drop while it gains kinetic energy in the stator, and then work is extracted through the rotor.

This analysis is based on the assumption that the flow follows streamlines aligned with the blade. Therefore, the algebraic expressions have been historically used for the mid-span of the blades, where this assumption is generally true. However, due to the presence of secondary flows at the tip of the blades, the analysis becomes more complex. As a result, CFD tools have gained popularity to study these complex flow cases.

All information in this section has been taken from [19].

2.4.3 Secondary Flow Losses in Turbomachinery

As it was introduced in the first chapter's Background and Motivation section, secondary flows are understood as deviations from the primary flow pattern. They play a significant role in turbomachinery losses, accounting for up to 30% of the energy losses [1]. These flows provoke losses by perturbing the flow field, increasing turbulence and mixing, which result in increased energy dissipation. Several factors contribute to vortex formation, the main mechanisms of secondary flow generation are the following:

- **Blade Geometry and Wakes:** Variations in blade curvature and twist can lead to the formation of

secondary flows, such as corner flows. As the fluid flows over the compressor blades, it creates wakes behind them. When subsequent blades encounter these wakes, they experience non-uniform flow, which also contribute to the creation of secondary flows.

- **Flow Separation:** Due to the effects of viscosity, a boundary layer is created on the surface of the blades. At specific blade sections, the boundary layer can separate from the blade surface. Flow separation can generate vortices as the flow reattaches downstream. The reattachment process creates swirling motions and vortical structures, which increase mixing and energy dissipation..
- **Interactions with the Casing:** The flow over the endwall surface develops a boundary layer. The interaction of this boundary layer with the primary flow motion can induce vortical structures.
- **Tip Clearance:** The necessary gap between the rotating and non-rotating parts, i.e. between rotor and endwall and between stator and shaft, creates additional flow paths for the fluid. This gap allows the flow to pass from the pressure to the suction side, generating tip leakage vortices (TLV) in the process. These structures wrap around the blade tip. They are the main source of secondary flow energy losses in compressor cascades.
- **Induced Vortices:** The interaction of strong vortices, such as the TLV vortices, with the surrounding flow field, can induce additional vortices.

Figure 2.2 illustrates the main vortical structures that can be found in the flow field around a compressor blade. The subfigure (a) shows the vortices found for a stationary endwall, and subfigure (b) shows the vortices found for an endwall with relative motion in the pitch-wise direction. These vortices have been identified using the λ_2 criterion. These images have been taken from [20], see the original paper for more information.

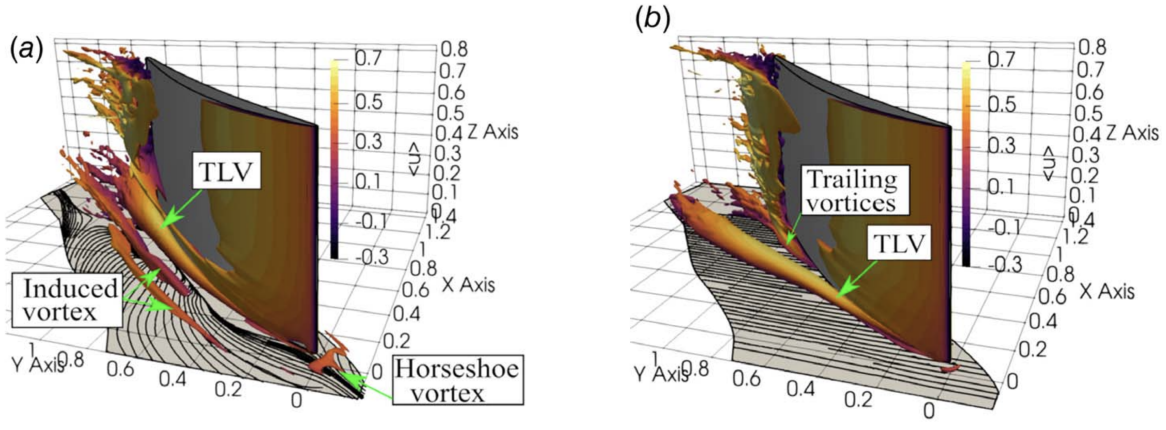

(a) Fixed Endwall (b) Endwall with Relative Velocity

Figure 2.2: Main Vortical Structures Found in Compressor Blades. Images Taken from [20]

.

The trailing edge vortices wrap around the blade tip, and their interaction with the surrounding flow generate additional parallel induced vortices, see figure 2.2a. The horseshoe vortices are flow structures that appear near the leading edge of the compressor blades for the stationary endwall case. These vortices are a result of

the interaction between the high-pressure region at the leading edge and the casing endwall. Lastly, for cases where the endwall has a relative speed, additional smaller vortical structures are found near the trailing edge of the blade due to the separation of the tip leakage vortex from the blade surface. This case is shown in figure 2.2b. It is important to clarify that the present study does not provide results for walls exhibiting relative motion. The description of this case was provided solely to illustrate the different kinds of vortices that can appear in turbomachinery compressors.

Chapter 3

Baseline Case

3.1 Geometry Definition and Methodology

The studied geometry consists on a linear cascade setup, composed by typical high-pressure compressor blade profiles. The blade profile and the fluid domain have been taken from the Chair of Turbomachinery and Flight Propulsion of TU Dresden setup [20]. The profile has a chord length of $c = 159.6\ mm$ and is positioned with a stagger angle of $46.9deg$ with respect to to the x axis, resulting in an axial chord length of $c_{ax} = 109.05\ mm$. The fluid domain is extruded from the xy plane with a height of $z/c_{ax} = 0.7$. The endwall is located at the bottom of the computational domain, at $z = 0$. And the gap between the sidewall and the blade tip has a size of $s/c_{ax} = 4.39\%$. All the simulations have been carried out using a Reynolds number of $Re = 10^4$, based on the axial chord and inlet velocity. The figure 3.1 shows the studied geometry's top plane view:

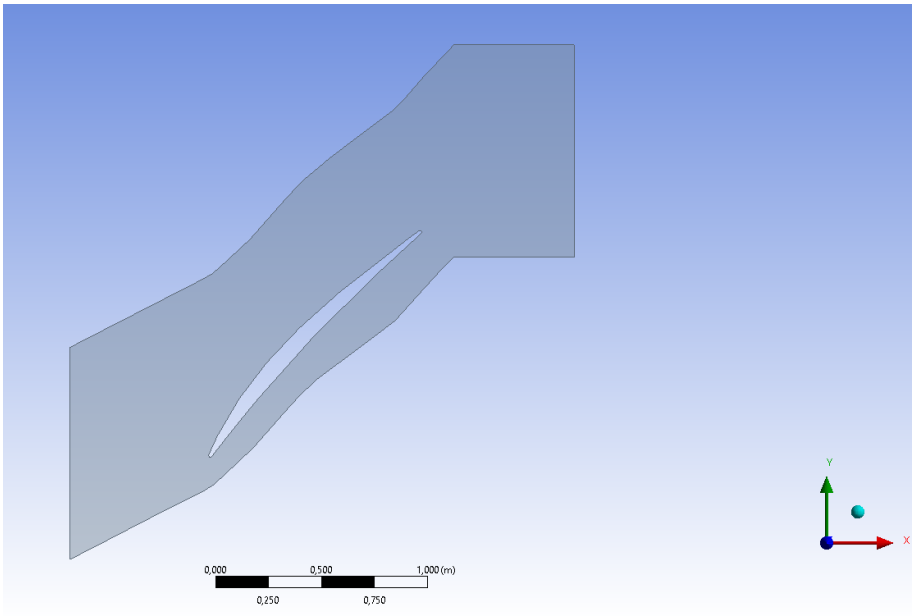

Figure 3.1: Geometry Front View

The Ansys Students software package will be used for both mesh generation and case simulation. The GEKO model of the Fluent solver will be employed. This solver requires dimensional inputs, therefore, the desired Reynolds number will be achieved by setting the density to $\rho = 1$ and fixing the inlet velocity magnitude to $\|\vec{u}\| = 1$. As a result, the Reynolds number can be adjusted by modifying the dynamic viscosity.

The methodology employed in this study involves several steps. Initially, a two-dimensional mesh will be created, and a mesh convergence analysis will be performed. Once convergence is achieved, the GEKO coefficients' sensitivity will be assessed by considerably modifying their values. Although the effects of the sidewall gap will not be observed in this particular case, this approach will yield rapid results and will provide a preliminary understanding of how the GEKO coefficients impact the critical parameters in the study. Subsequently, the mesh will be extruded to obtain a three-dimensional domain that incorporates the gap. The three dimensional case will be simulated with the calibrated values obtained in the two dimensional analysis. Finally, the calibrated model will be compared with the default GEKO setup and the standard $k - \omega$ model.

3.2 General 2D Flow Description

This section provides a description of the flow around the blade in the two dimensional case. The flow enters the domain via the **INLET**, coloured in dark blue in figure 3.2, and exits it via the **OUTLET**, coloured in red. Both the **BOTTOM** and **TOP** sections, coloured in black and magenta respectively, are periodic regions. This means that the flow entering the **TOP** region, exits by the **BOTTOM** region and vice-versa. As it can be seen in figure3.2a, a higher velocity magnitude is obtained at the suction side comparing it to the pressure side. This velocity variation provokes a pressure difference between the both sides of the blade, as it is illustrated in figure 3.2b. Consequently, a net lifting force is obtained.

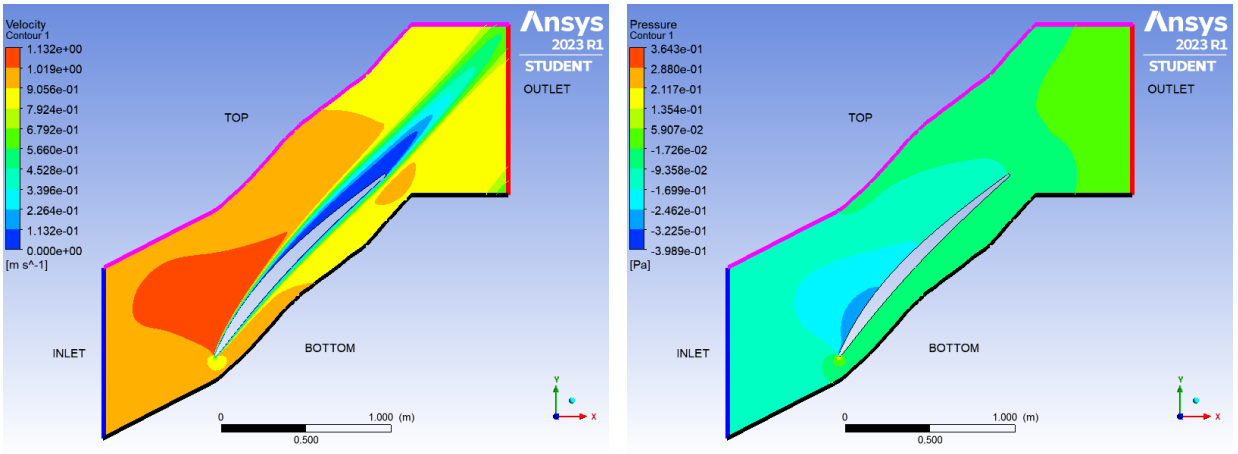

(a) Velocity Magnitude (b) Pressure Magnitude

Figure 3.2: Velocity and Pressure Magnitude Fields

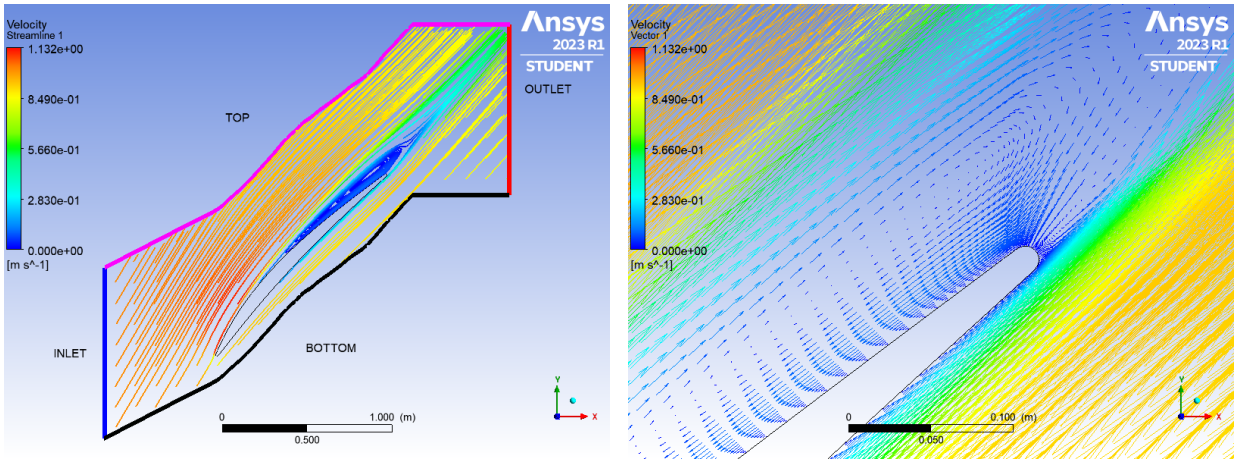

(a) Velocity Stream Lines (b) Velocity Vector Field

Figure 3.3: Velocity Stream Lines and Vectors

The blade provokes a wake region near its trailing edge, see figure 3.2a, considerably slowing down the fluid's velocity. Due to the effects of boundary layer separation, a recirculation zone forms near the trailing edge. This zone is illustrated by plotting stream lines, and velocity vector fields in figures 3.3a and 3.3b. Simulation results will be assessed by evaluating critical parameters such as the pressure coefficient, lift coefficient, skin friction coefficient, and total pressure loss coefficient.

These parameters are defined as follows:

- **Pressure Coefficient:** The pressure coefficient is a dimensionless parameter that characterizes the relative pressure distribution across a flow field. It is defined as follows:

$$c_p = \frac{(< p > - p_1)}{\frac{1}{2}\rho \|u_1\|^2} \tag{3.1}$$

  For the study case, p_1 is the pitchwise-averaged inlet pressure and $\|u_1\|$ is the inflow velocity magnitude.

- **Skin Friction Coefficient:** The skin friction coefficient is a dimensionless quantity that represents the shear stress between a fluid and a solid surface. This parameter is useful to assess the boundary layer behaviour. It is defined as follows:

$$c_f = \frac{\tau_w}{\frac{1}{2}\rho \|u_1\|^2} \tag{3.2}$$

  where τ_w is the wall shear stress.

- **Lift Coefficient:** The lift coefficient is a dimensionless parameter that quantifies the amount of lifting force generated by an object in a fluid flow. In this case, it is obtained by calculating the area between the pressure and suction side's pressure coefficient's curves.

- **Total Pressure Loss Coefficient:** The total pressure loss coefficient characterizes the stagnation pressure losses between two sections of the fluid domain. This parameter is adimensionalized by the

dynamic pressure. It is defined as follows:

$$\zeta(x) = \frac{p_{t,ref} - p_t(x)}{p_{dyn,ref}} \tag{3.3}$$

For the study case, $p_{t,ref}$ and $p_{dyn,ref}$ are the total and dynamic pitchwise-averaged inlet pressure, and $p_t(x)$ is the pitchwise-averaged total pressure at $x = 1.3\ c_{ax}$.

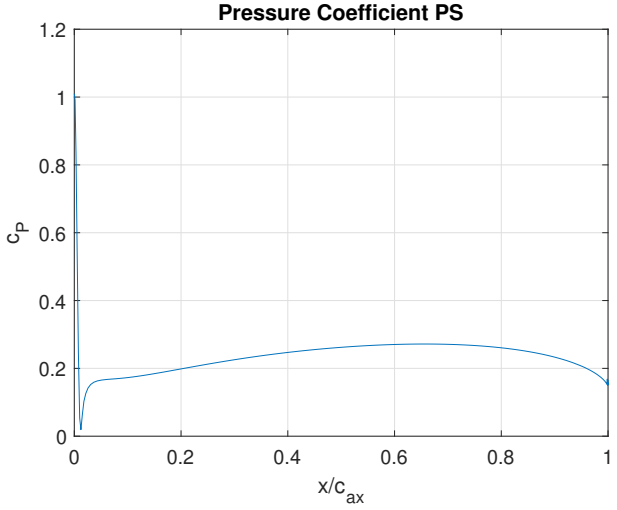

(a) c_f PS

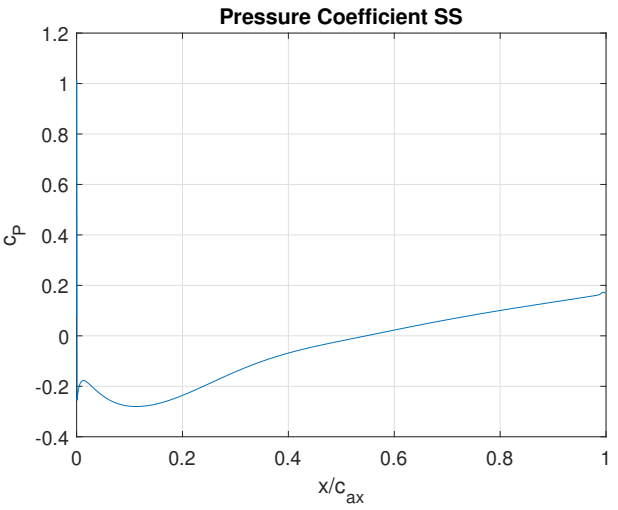

(b) c_f SS

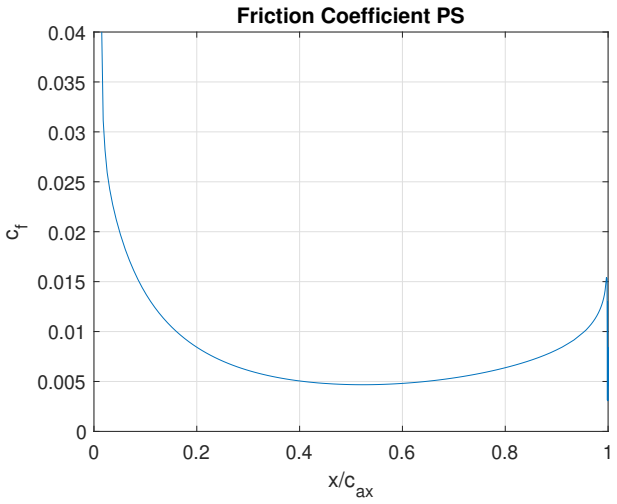

(c) c_f PS

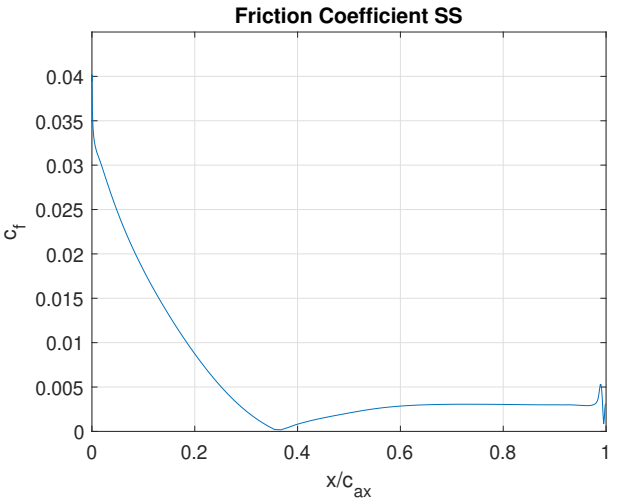

(d) c_f SS

Figure 3.4: Pressure and Friction Coefficient Plots for the General 2D Case

Figure 3.4 shows the pressure and skin friction coefficient's distribution across the axial chord for both the pressure and suction sides. Figure 3.4d shows how the skin friction coefficient of the suction side drops considerably at $c_{ax} = 0.36$, indicating boundary layer separation. This effect could also be seen in figures 3.2 and 3.3. On the other hand, from figure 3.4c, it can be seen that the boundary layer at the pressure side remains attached throughout the axial chord. Additionally, the boundary layer state of the suction side will also be characterized by turbulent kinetic energy distribution plots, see figure 3.5. The vertical axis

represents the perpendicular distance from the wall normalized by the axial chord, and the horizontal axis represents position normalized by the axial chord plus four times the turbulent kinetic energy magnitude. This figure also shows how the turbulent kinetic energy increases in the recirculation zone.

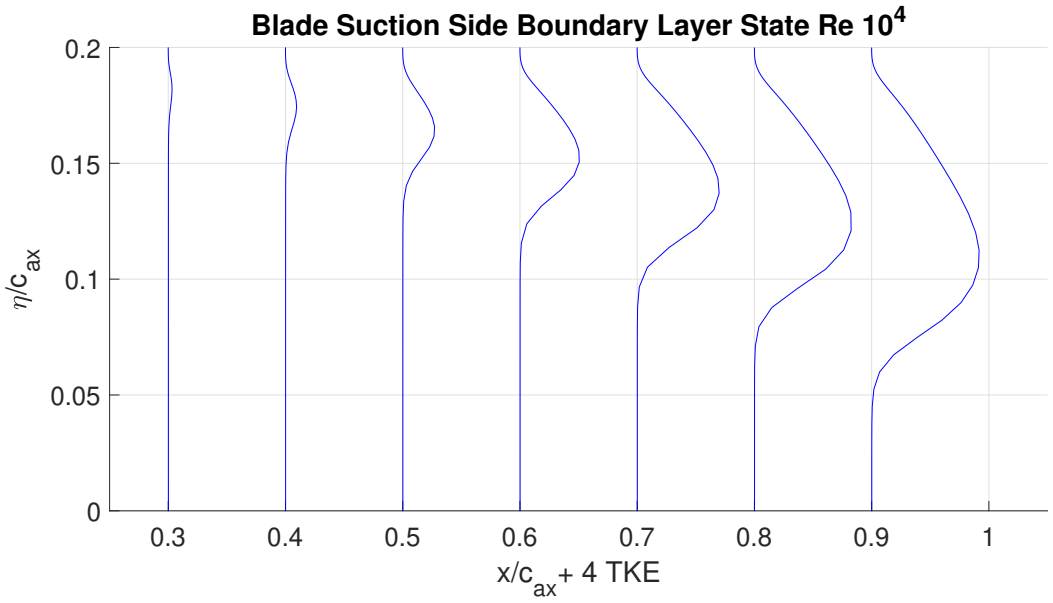

Figure 3.5: Boundary Layer State

3.3 2D Meshing and Boundary Conditions

For the two dimensional case, a multi-zone structured mesh approach has been employed. A structured mesh consists on a grid where the cells are regularly shaped, such as rectangles or hexahedrons. These cells are aligned with the geometry of the problem, interconnected in a systematic manner, and arranged in a well-defined pattern. Therefore, in a two dimensional structured mesh, the cells can be identified as i, j elements inside a matrix. A multi-zone structured mesh consists of multiple interconnected structured blocks. This approach allows for the mesh to be selectively refined in critical blocks.

Given the shape of the airfoil and the domain, it had been determined that an O-grid mesh would be suitable for the surroundings of the blade profile. This mesh type consists of two sets of lines: one set of grid lines run parallel to the airfoil walls, and the other set of lines run perpendicular. When viewed from a frontal perspective, an O-grid mesh resembles an oval. However, in this particular case, due to the necessary intermediate blocks to smoothly interconnect the different regions, this oval shape cannot be appreciated. In order to structure the mesh, all blocks must be quadrilateral, and this was a challenge. Due to the complex geometry of the fluid domain, it was not feasible to mesh the entire domain as an O-grid, since additional blocks were required at the corners to smoothly interconnect the different regions. Figure 3.6 shows the meshing blocks:

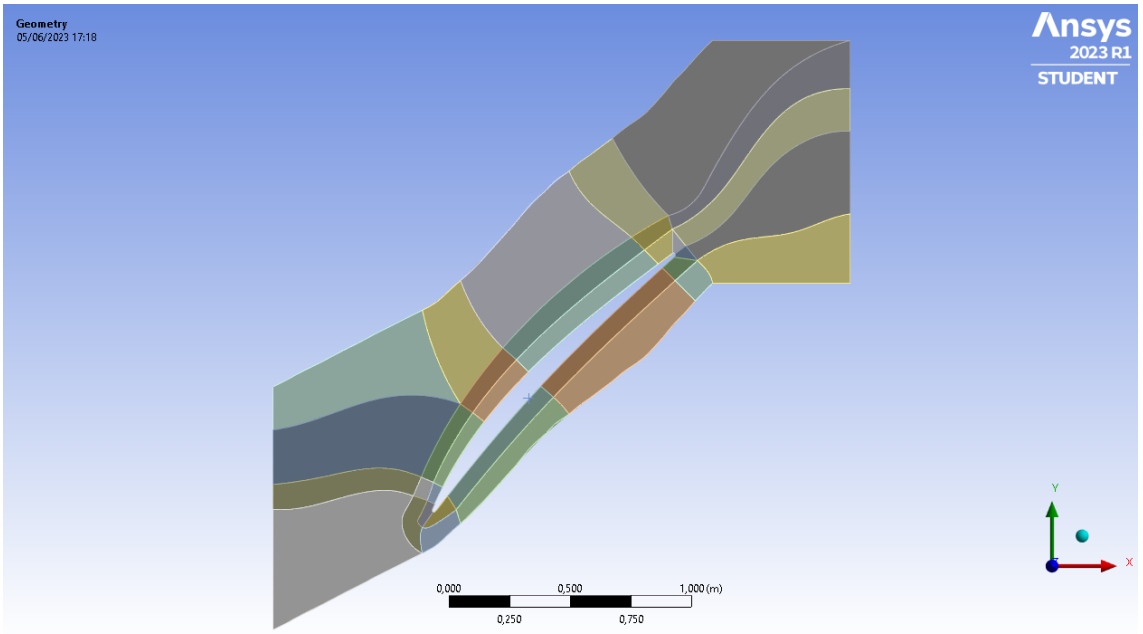

Figure 3.6: Meshing Blocks

There are multiple layers of blocks surrounding the blade profile. There are two layers for the pressure side, and three for the suction side. The suction side requires more layers due to the larger fluid area to be meshed. Each layer has a different growth rate, with the first layer having the smallest growth rate. In order to separate the fluid domain into different blocks, splines have been traced. These splines are perpendicular at edge intersections to minimize cell skewness. However, it should be noted that at the top right corner of the fluid domain, the cells have a higher skewness (see figure 3.7). The impact of these lower quality cells has been found to be minimal.

The first layer cells near the boundary of the profile have a height of $y^+ < 1$. The cells at the leading and trailing edges have a higher y^+ value compared to those in the middle of the profile. Nevertheless, the y^+ value is still maintained below $y^+ = 1$ to ensure sufficient resolution to accurately resolve the boundary layer. This condition will allow the mesh to resolve the laminar part of the boundary layer without using wall models. The mentioned height variations are due to the differences in curvature at the leading and trailing edges. Prior to creating the definitive initial mesh structure, preliminary meshes were created to perform simulations and identify critical regions. For instance, after identifying the location of the wake region, additional refinement was implemented for that specific area to achieve a more accurate resolution. Figure 3.7 shows the initial mesh:

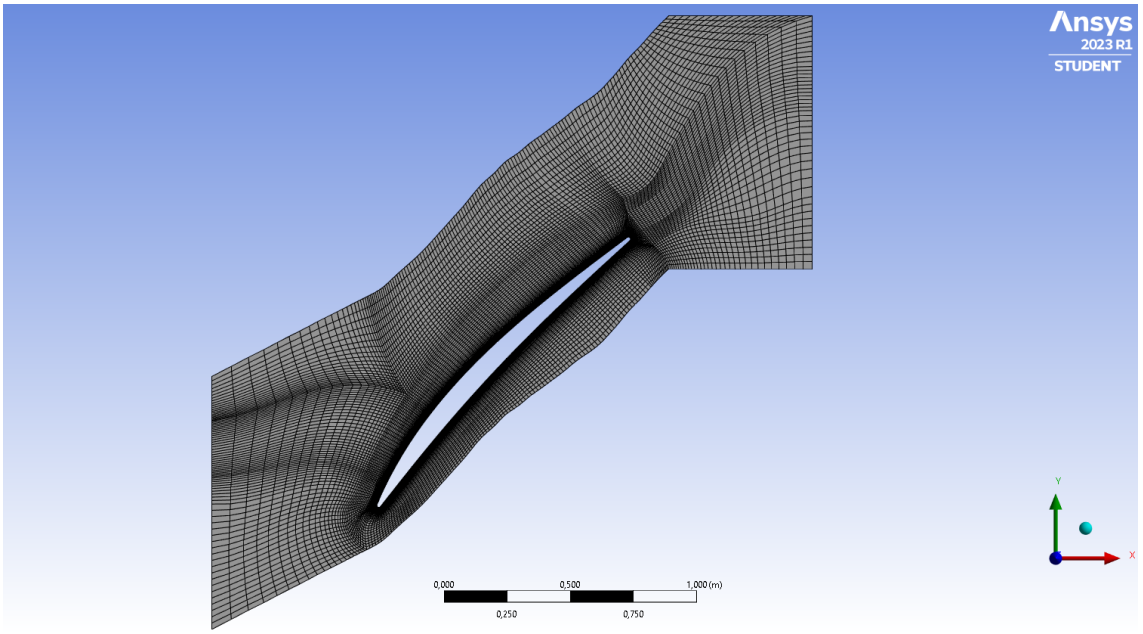

Figure 3.7: Initial Mesh

To simulate the linear blade cascade, periodic conditions have been set at the aforementioned bottom and top regions of the fluid domain. Although the ideal scenario is to have an identical mesh at the periodic zones, this has not been achieved due to the complex geometry of the case. The bottom and top regions have the same number of elements until reaching the horizontal region near the blade's trailing edge.The solver will interpolate values to establish the periodic condition, and some error may be introduced.

The profile boundaries have been set to no slip walls, this implies that the fluid velocity at these boundaries is zero. The exit of the fluid domain has been specified as a pressure outlet boundary condition, ensuring that the flow exits the computational domain without any back-flow. A constant velocity of magnitude $\|\vec{u}\| = 1$ with components $u = 0.5150381$ and $v = 0.8571673$ has been imposed at the inlet. These inflow velocity components will change for the three dimensional case. These values were provided by the project's director. They account for correction factors from the conversion from the 3D case. Lastly, at the inlet, a turbulent intensity of 1% and a turbulent length scale of $5mm$ [21] have been enforced. The turbulence-related boundary conditions at the inlet will be assessed at a later stage to study their influence.

3.4 Mesh Convergence Study

To evaluate the influence of the mesh density on the results, the original mesh has been systematically modified by creating additional meshes by increasing and decreasing the total number of elements. The methodology employed for the generation of these new meshes involved adjusting the number of elements along two different directions: one parallel and the other perpendicular to the blade profile. It is important to highlight that the y^+ values of cells adjacent to the profile have not been changed throughout the mesh modifications. All the meshes have been adjusted to ensure a $y^+ < 1$. In addition to adjusting the number of elements along each direction, the growth rates have also been modified to achieve smooth mesh transitions.

At first, the base mesh size had been doubled and halved. For the mesh size increment, three different meshes were created: one by doubling the number of elements along the parallel direction, another by doubling along the perpendicular direction, and a third by multiplying the number of elements in both directions by $\sqrt{2}$. For the mesh size reduction, two meshes were created by halving the number of elements in either the parallel or the perpendicular directions, and another one was created by dividing the number of elements in both directions by $\sqrt{0.5}$.

Furthermore, a few more meshes were created by increasing and decreasing both direction's elements: a mesh with 4 times the number of elements of the base mesh, by doubling the number of elements along both directions; another one with 16 times the number of elements of the initial mesh, by multiplying by 4 the number of elements along both directions; another with 0.25 times the number of elements of the base mesh, by halving the number of elements along both directions; and finally one with 0.125 times the number of elements of the base mesh, by dividing the number of elements along both directions by 4. In order to characterise the effect of the mesh on the results, the lift coefficient and the total pressure loss coefficient were used to analyse the convergence. Figures 3.8 and 3.9 show the pressure and friction coefficient distribution along the axial chord. Even though details cannot be appreciated since the lines overlap each other, it can be seen that all the meshes provide similar results along the blade profile due to the maintained y^+.

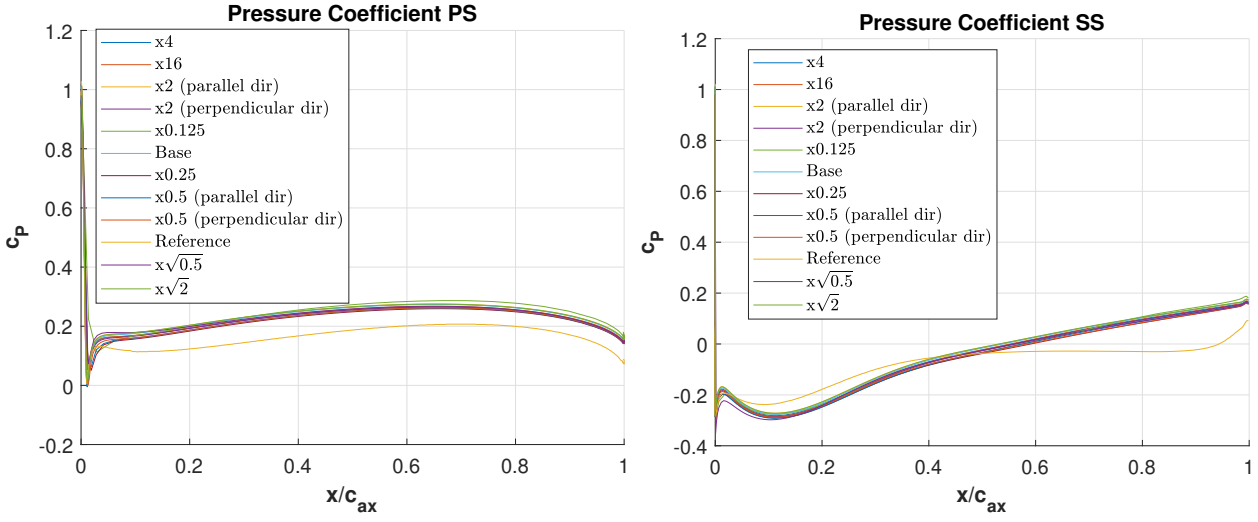

(a) c_p PS (b) c_p SS

Figure 3.8: Friction Coefficient Plots for all the Meshes

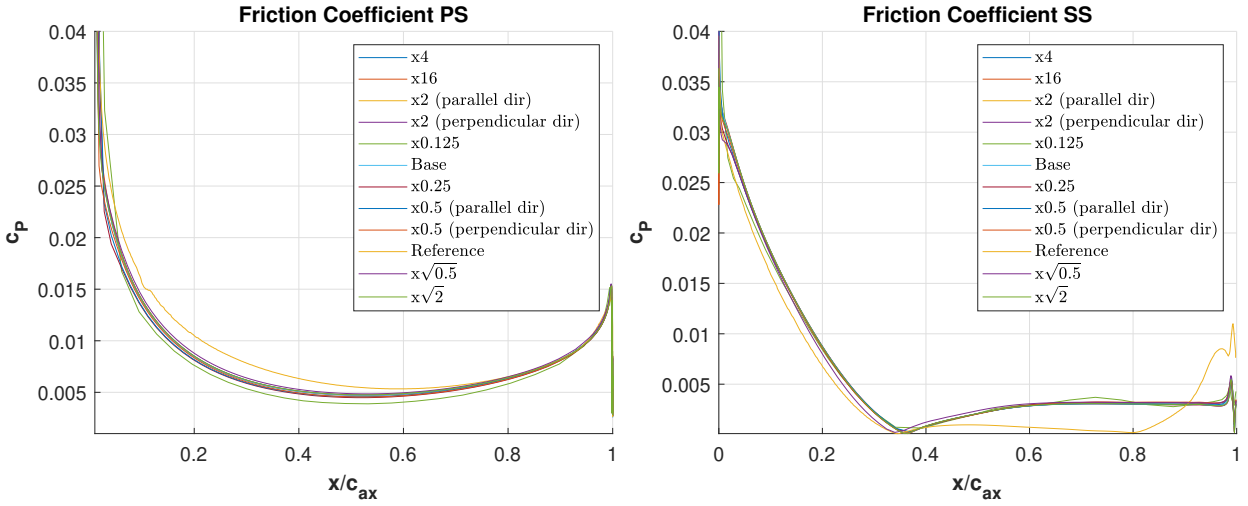

(a) c_f PS (b) c_f SS

Figure 3.9: Friction Coefficient Plots for all the Meshes

From the results depicted in figures 3.8 and 3.9, it is clear that the RANS simulations achieve to capture the overall tendencies of the flow with respect to the Reference data, even if they do not provide exact values. There is a slight offset in the pressure side's pressure coefficient distribution, but the tendency is well captured. On the other hand, the pressure coefficient at the suction side presents deviations from the reference data for $x/c_{ax} > 0.4$, where the reference curve is flattened and starts to increase again at $x/c_{ax} = 0.9$. Regarding the skin friction coefficient, the tendencies have been accurately captured for the pressure side, and the values are also close to the reference data. On the other hand, the suction side presents a higher friction coefficient from $x/c_{ax} > 0.4$ in the RANS simulations, indicating thicker boundary layers. The higher friction coefficient near the trailing edge ($x/c_{ax} > 0.8$) of the reference data indicating flow reattachment, is not well captured by the RANS simulations. The thicker boundary layer predicted by the RANS simulations can be attributed to the inherent dissipative behaviour of the its formulation.

The following table shows the results obtained with all the meshes:

Mesh	Elements	Lift Coefficient	Total Pressure Loss Coefficient
x0.125	1039	0.2911	0.0876
x0.25	3605	0.2785	0.0739
x0.5 (perpendicular dir)	7088	0.2783	0.0723
x0.5 (parallel dir)	7357	0.2780	0.1034
x0.5 (both dir multiplied by $\sqrt{0.5}$)	7589	0.2862	0.1284
Original Mesh	14948	0.2757	0.1250
x2 (parallel dir)	27972	0.2752	0.1169
x2 (perpendicular dir)	33208	0.2743	0.1179
x2 (both dir multiplied by $\sqrt{2}$)	34003	0.2742	0.1228
x4	61616	0.2754	0.1110
x16	246464	0.2777	0.1101

Table 3.1: Mesh Convergence Study Results

The orange and yellow coloured cells represent similar size jumps. Since the mesh has been refined on different directions for the x0.5 and x2 size jumps, the convergence will be studied in three different directions. Figure 3.10 illustrates the convergence along the different directions. The lift coefficient does not exhibit strong variations across the different meshes. These results indicate that this parameter is not very sensitive to mesh resolution. On the other hand, the total pressure loss coefficient presents significant variations. For the total pressure loss coefficient convergence graphs, the first size jump has lower relative changes than the second one. This is due to the fact that the mesh is still not fine enough to correctly resolve the boundary layer. Once the third size jump is reached, the relative changes start to decrease because the mesh reaches enough resolution to resolve the critical regions.

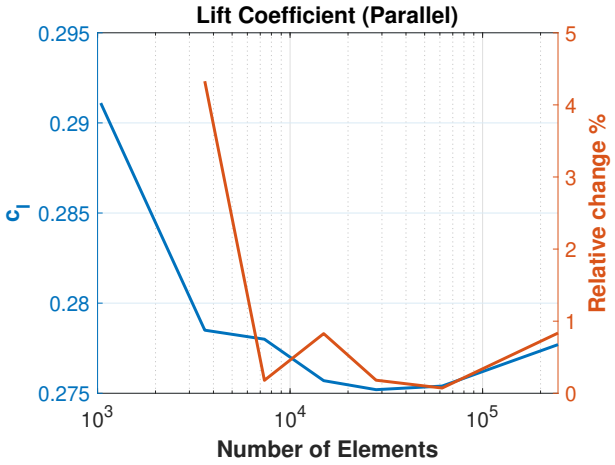

(a) Lift Convergence (Parallel Dir)

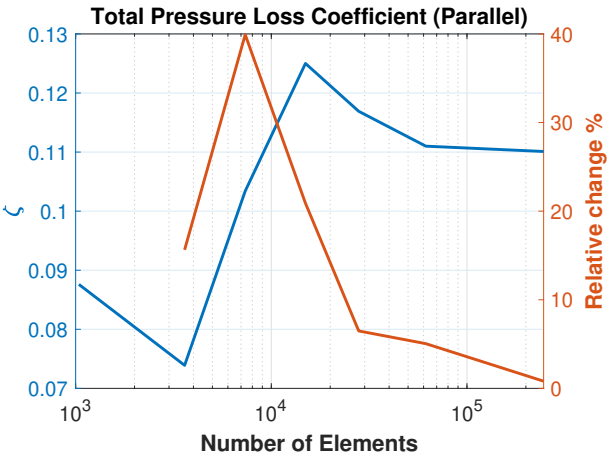

(b) Total Pressure Loss Convergence (Parallel Dir)

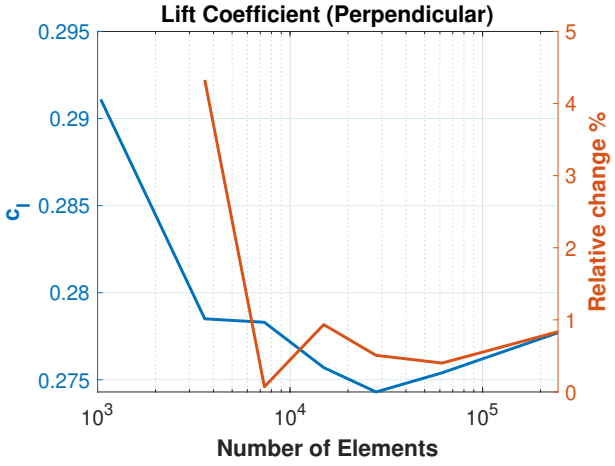

(c) Lift Convergence (Perpendicular Dir)

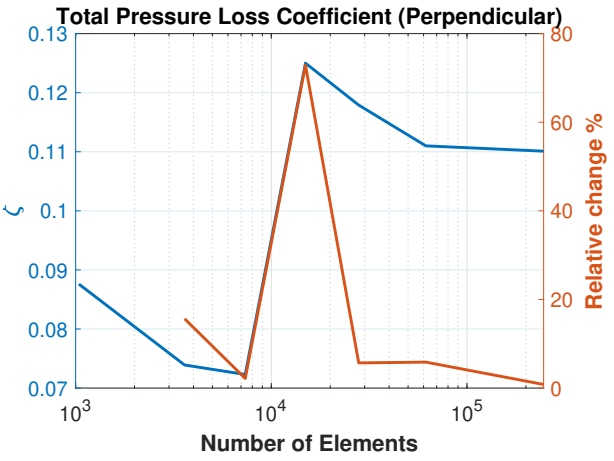

(d) Total Pressure Loss Convergence (Perpendicular Dir)

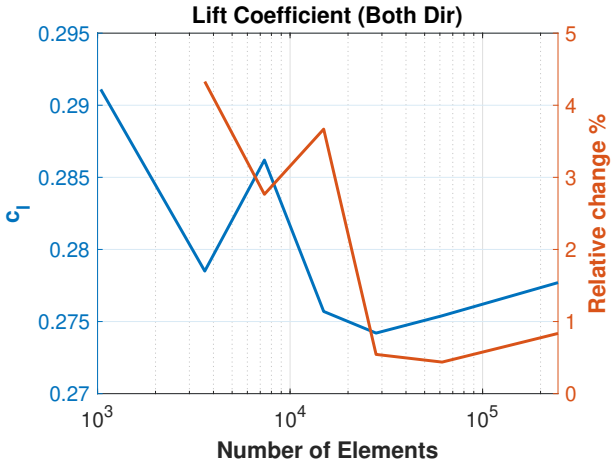

(e) Lift Convergence (Both Dir)

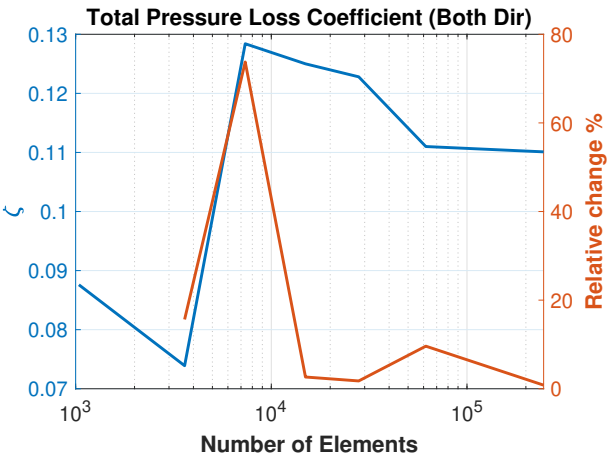

(f) Total Pressure Loss Convergence (Both Dir)

Figure 3.10: Mesh Convergence Plots

3.5 Inlet Boundary Condition Calibration

Although the total pressure loss and lift coefficients have converged, the total pressure loss value does not match the reference value: $\zeta = 0.1339$ taken from [22]. In order to achieve the desired value, the inlet boundary conditions will be modified. The case will be simulated using the original mesh and varying the turbulent length scale. Table 3.2 shows the total pressure loss coefficient variations.

Turbulent Length Scale (m)	Total pressure Loss Coeff
1e-1	0.1165
1e-2	0.1222
5e-3 (original)	0.1250
1e-3	0.1313
1e-4	0.1355

Table 3.2: Inlet Boundary Condition Calibration

The turbulent length scale of $10^{-3}m$ is the one closest to the reference value, and will be used in the three-dimensional simulation. The $10^{-4}m$ length' result is also close, but in this case, the simulation was not stable, and the residuals started to oscillate. Figures shows 3.11 and 3.12 show 2D contours of the velocity magnitude field for the different turbulent length scales. From this contours, the main difference that can be appreciated from the different inlet boundary conditions is the velocity below the pressure side. As the turbulent length scale decreases, the velocity magnitude increases in the region below the pressure side for $x/c_{ax} < 0.5$. A velocity magnitude increase near the trailing edge can also be appreciated.

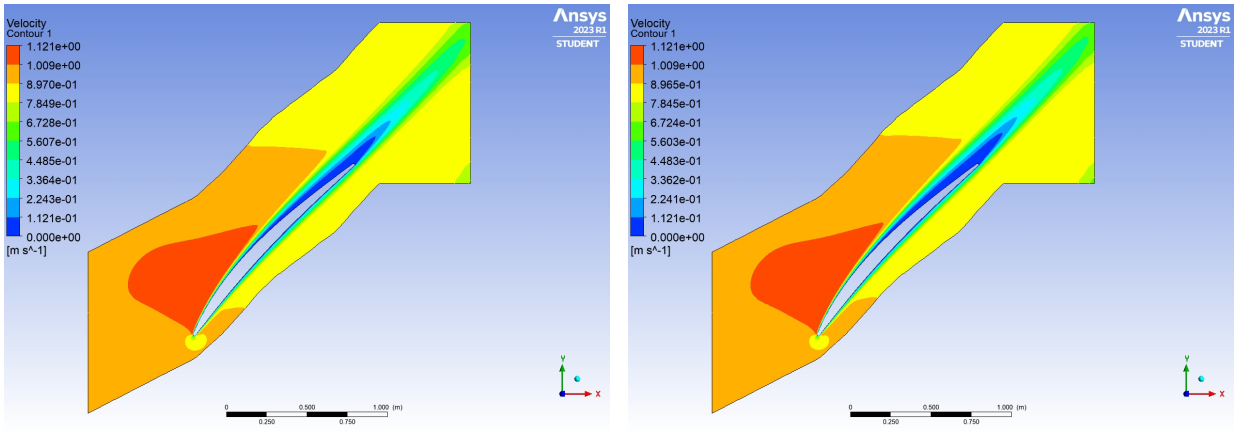

(a) Turbulent Length Scale of $10^{-1}m$ (b) Turbulent Length Scale of $10^{-2}m$

Figure 3.11: Velocity Magnitude Contours for different Turbulent Length Scales. Subfigures a and b

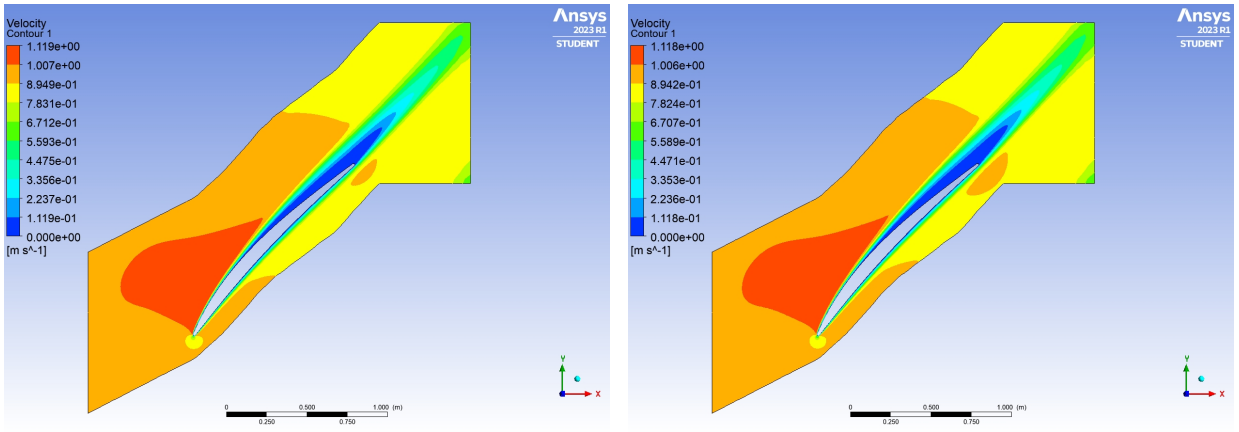

(a) Turbulent Length Scale of $10^{-3}m$ (b) Turbulent Length Scale of $10^{-4}m$

Figure 3.12: Velocity Magnitude Contours for different Turbulent Length Scales. Subfigures c and d

3.6 GEKO Coefficient Calibration

In this section, the GEKO coefficients will be modified one by one to assess their influence in the study case. The base mesh will be used for the next simulations, since it strikes a balance between accuracy and simulation time. The base boundary condition of turbulent length scale of $5 \cdot 10^{-3}$ will be used, and all the other boundary conditiones will remain the same. Only the CSEP, CNW, and CJET coefficients will be modified. The CMIX coefficient is automatically calculated from the CSEP coefficient as mentioned in the previous chapter.

All the parameters have been modified significantly, but within a reasonable range, following the guidelines set by Ansys [18]. A unique simulation was run for each parameter change, while mantaining all the other parameters to their default value. The CSEP values were 1, 1.75, 2.5; the CNW values were 0.25, 0.5, 0.75; and lastly the CJET values were 0.45, 0.9, 1.35.

Table 3.3 shows how much the parameters change respect to the reference values. The reference values for the lift, pressure, and friction coefficients have been taken from plot integrals from the data in [20]. Green coloured cells are bellow the reference value, red coloured ones are above, and yellow cells are close to the reference. For each GEKO coefficient, the "Min","Default", and "Max" rows refer to the three values for each coefficient aforementioned. The colouring of each table has been set in a manner that the values closer to the reference are coloured in yellow. Different colouring approaches were experimented, and these were the methods that created a visual colour gradient effect that helped analysing the parameter's behaviour.

CP_PS_Int	Min	Default	Max
CSEP	0.3097 (82.9%)	0.2843 (67.9%)	0.2894 (70.9%)
CNW	0.2844 (68.0%)	0.2843 (67.9%)	0.2843 (67.9%)
CJET	0.2842 (67.9%)	0.2843 (67.9%)	0.2822 (66.7%)

Pressure Coefficient Curve Integral Along PS

Reference Value is 0.1693

CP_SS_Int	Min	Default	Max
CSEP	-0.0760 (-6.2%)	0.0086 (109.88%)	0.0023 (102.8%)
CNW	0.0086 (109.88%)	0.0086 (109.88%)	0.0087 (110.7%)
CJET	0.0090 (111.1%)	0.0086 (109.88%)	0.0215 (126.5%)

Pressure Coefficient Curve Integral Along SS

Reference Value is -0.081

CF_PS_Int	Min	Default	Max
CSEP	0.0088 (-11.1%)	0.0094 (-5.1%)	0.0092 (-7.1%)
CNW	0.0094 (-5.1%)	0.0094 (-5.1%)	0.0094 (-5.1%)
CJET	0.0094 (-5.1%)	0.0094 (-5.1%)	0.0098 (-1%)

Friction Coefficient Curve Integral Along PS

Reference Value is 0.0099

CF_SS_Int	Min	Default	Max
CSEP	0.0062 (24.0%)	0.0065 (30.0%)	0.0064 (28.0%)
CNW	0.0065 (30.0%)	0.0065 (30.0%)	0.0065 (30.0%)
CJET	0.0065 (30.0%)	0.0065 (30.0%)	0.0064 (28.0%)

Friction Coefficient Curve Integral Along SS

Reference Value is 0.005

CL	Min	Default	Max
CSEP	0.3857 (49.2%)	0.2757 (6.7%)	0.2871 (11.1%)
CNW	0.2758 (6.7%)	0.2757 (6.7%)	0.2756 (6.6%)
CJET	0.2752 (6.5%)	0.2757 (6.7%)	0.2607 (0.9%)

Lift Coefficient

Reference Value is 0.2585

Total_P_Loss	Min	Default	Max
CSEP	0.1027 (-23.3%)	0.1250 (-6.6%)	0.1170 (-12.6%)
CNW	0.1250 (-6.6%)	0.1250 (-6.6%)	0.0993 (-25.8%)
CJET	0.1252 (-6.6%)	0.1250 (-6.6%)	0.1348 (0.7%)

Total Pressure Loss Coefficient

Reference Value is 0.1339

Table 3.3: GEKO Parameters Comparison Respect to Reference Values

-80	-40	0	+40	+80

CP_PS_Int

-10	-5	0	+5	+10

CF_PS_Int

-50	-25	0	25	+50

CL

-110	-55	0	55	+110

CP_SS_Int

-25	0	25	+50	+75

CF_SS_Int

-20	-10	0	+10	+20

Total_P_Loss

Table 3.4: Colouring Legend for Each Table

When examining the pressure coefficient integrals, a large difference across all cases is observed with respect to the reference value. This discrepancy arises due to an offset in the pressure coefficient curves. For this case, by reducing the CSEP value from its default setting, the boundary layer's transition from laminar to turbulent flow is initiated at a lower axial chord coordinate, see figure 3.13c. This results in a lift coefficient overestimation, since a larger part of the airfoil's suction side experiences a laminar flow. As it was mentioned in the previous chapter, this is a consequence of the reduced sensitivity to adverse pressure gradients within the boundary layer resulting from the reduced CSEP coefficient. Figure 3.14 illustrates how the turbulent kinetic energy near the suction side wall starts growing faster along the axial chord for higher CSEP values.

The CNW parameter has negligible effects for the pressure coefficient integrals and the lift coefficient. However, increasing its value leads to a reduction in the total pressure loss coefficient. According to the Ansys documentation [18], an increase in this parameter results in a higher wall shear stress, and consequently this could delay separation of the boundary layer and decrease pressure losses. However, there has not been a change in the skin friction integrals nor the distribution curves, see figure 3.16. The Ansys documentation

states that its effects on vortices and wakes has not been tested yet, but from the obtained results it could be deduced that it is affecting the wake region by modifying the wake's size, since all the parameters considered along the blade have not changed.

By increasing the CJET parameter, the jet spreading rates are reduced according to the Ansys documentation. Although there are no jet flows in this case, this parameter can affect the mixing rates and shear free-flows. As it was described in the General 2D Flow description section, the study case presents a wake near the trailing edge. The CJET parameter affects the resolution of the wake region. The reduced jet spreading rates when the CJET's value is increased, decreases the overall performance of the blade by decreasing its lift coefficient, and provoking higher total pressure losses. Among all the considered parameters, the CJET parameter exhibited the most notable improvement in simulations by yielding results that closely matched the reference data.

The distribution of the pressure and friction coefficients, as well as the boundary layer behaviour can be found in figures 3.13, 3.16 and 3.17.

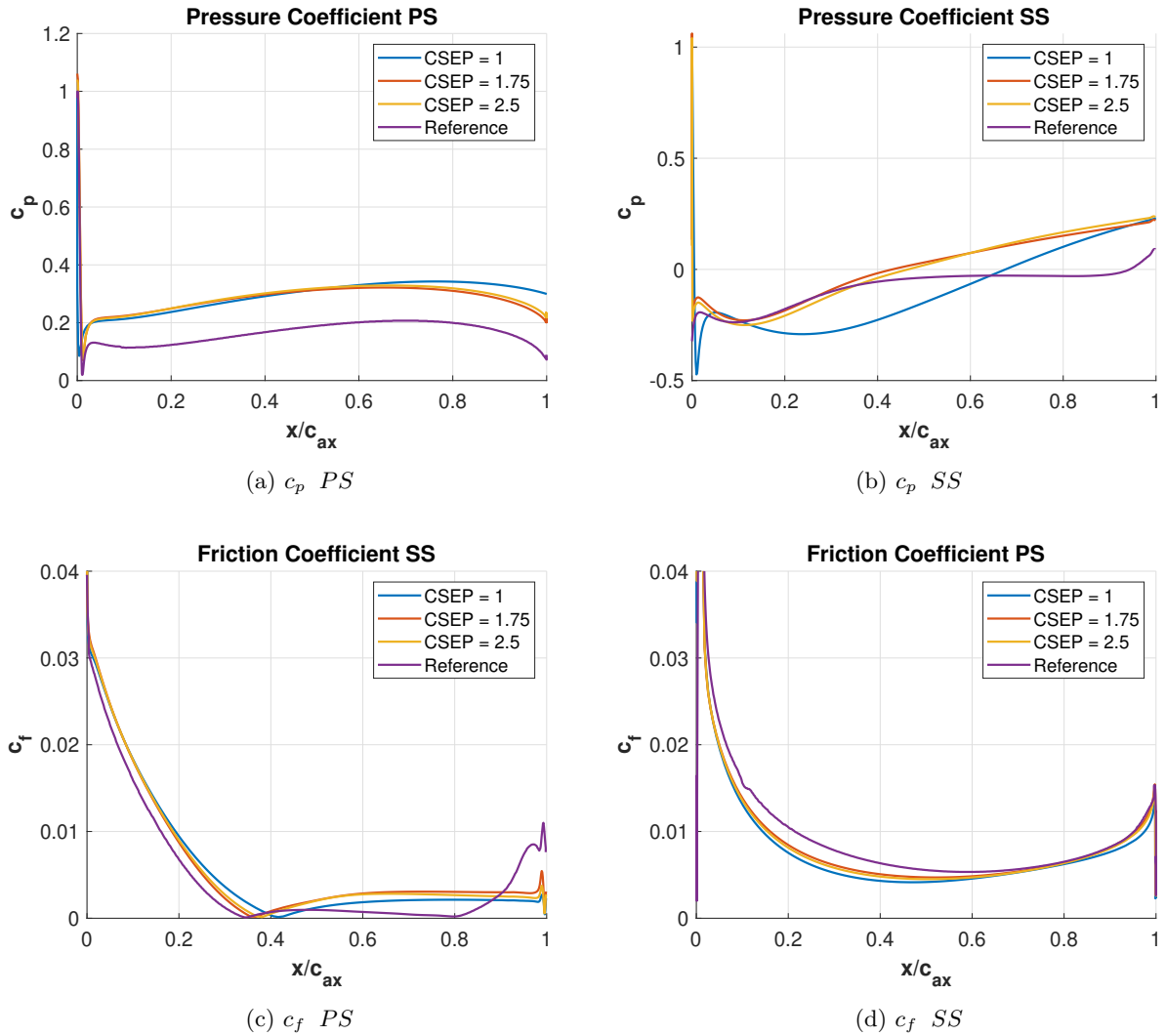

(a) c_p PS

(b) c_p SS

(c) c_f PS

(d) c_f SS

Figure 3.13: Pressure and Friction Coefficients for CSEP Variations

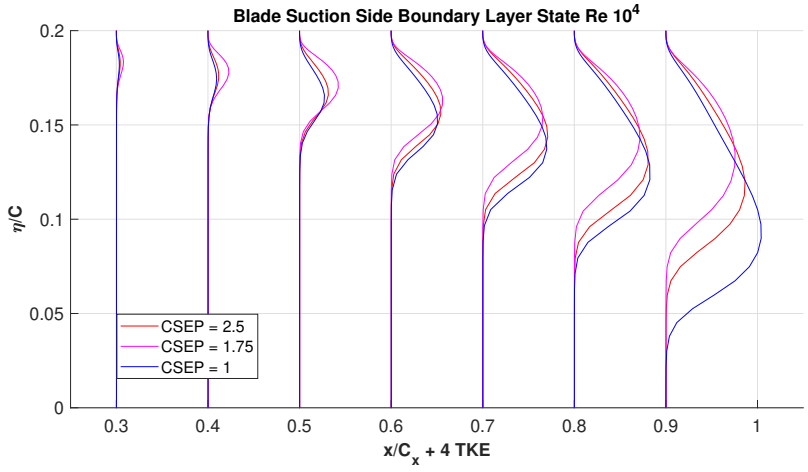

Figure 3.14: Boundary Layer State for CSEP Variations

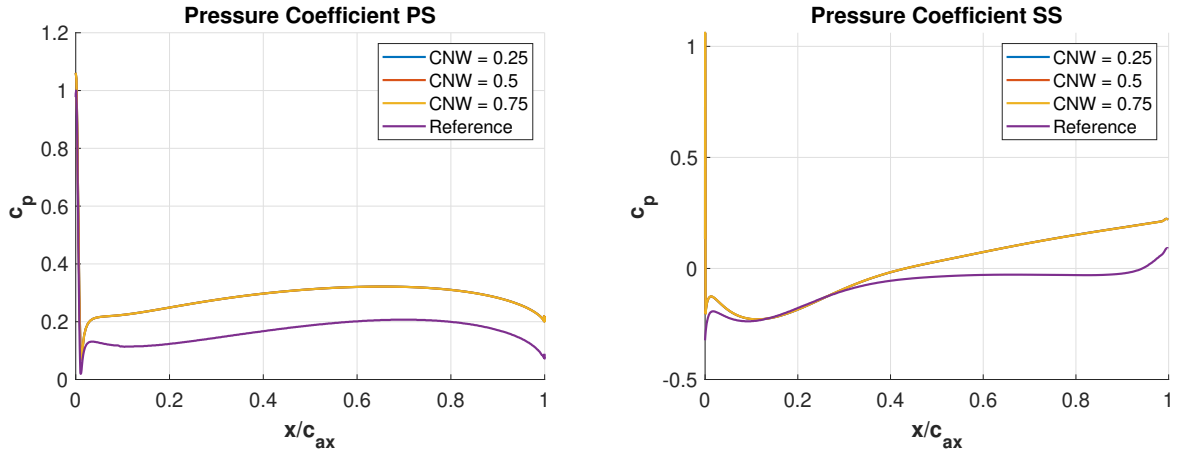

(a) c_p PS

(b) c_p SS

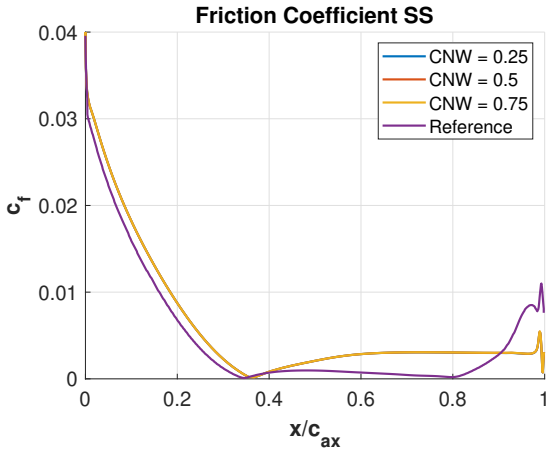

(c) c_f PS

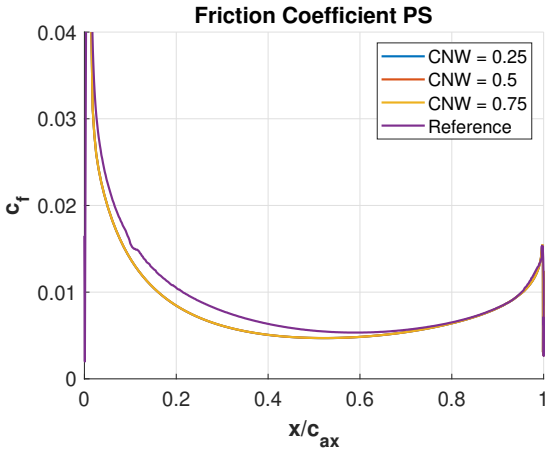

(d) c_f SS

Figure 3.15: Pressure and Friction Coefficients for CNW Variations

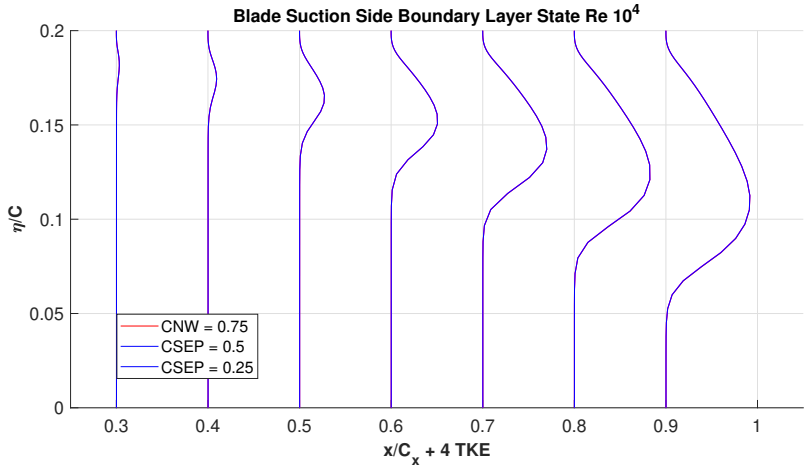

Figure 3.16: Boundary Layer State for CNW Variations

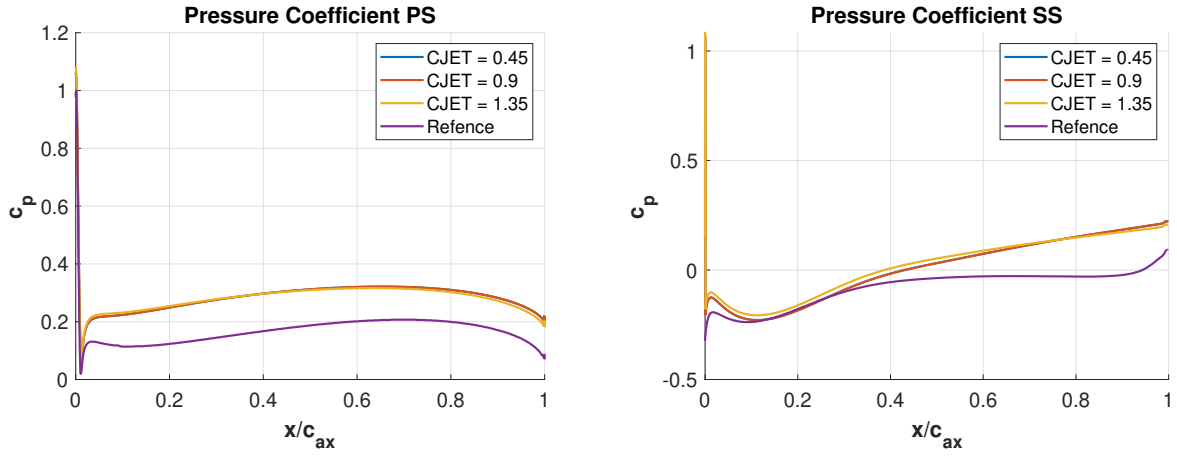

(a) c_p PS

(b) c_p SS

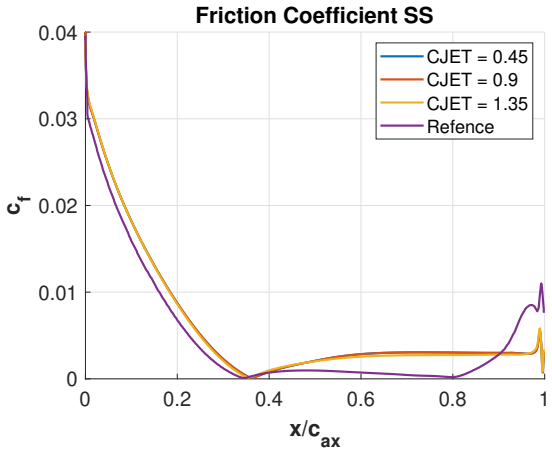

(c) c_f PS

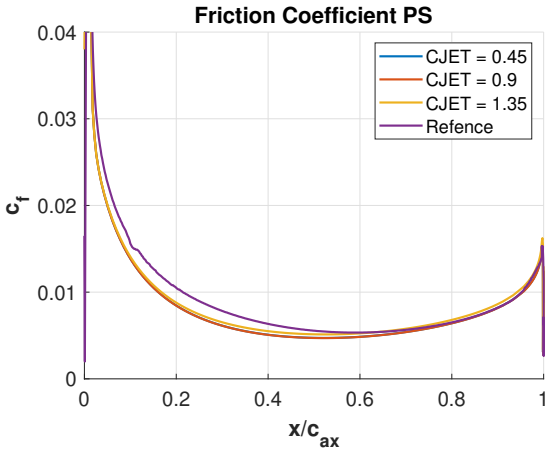

(d) c_f SS

Figure 3.17: Pressure and Friction Coefficients for CJET Variations

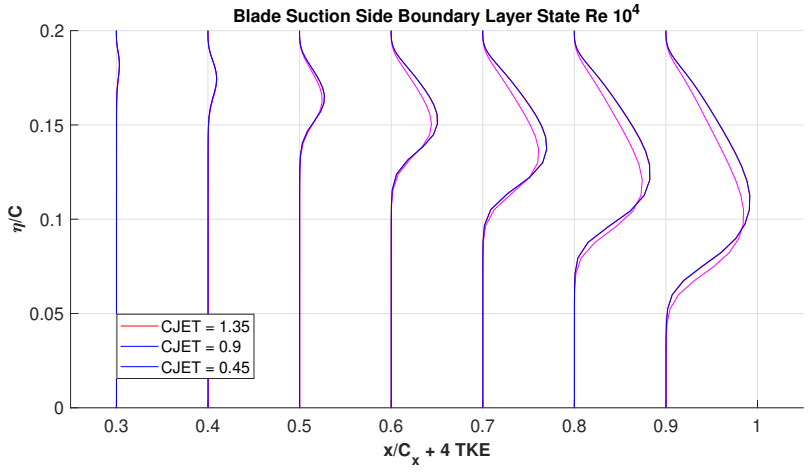

Figure 3.18: Boundary Layer State for CJET Variations

Chapter 4

Three Dimensional Case

4.1 General 3D Flow Description

Unlike the previous case, the three dimensional flow will be affected by the endwall and the casing's gap effects. When the flow reaches the leading edge of the blade, it undergoes a significant change in direction, and joined to the endwall' and the gap's effects, a horseshoe type vortex is formed. The pressure differences between the pressure and suction sides of the blade, create a net secondary flow that passes through the gap, see figure 4.1a. The flow passing through this gap generates a tip leakage vortex, which is one of the main sources of inefficiencies. Furthermore the strength of this vortex induces secondary parallel vortices. Figure 4.1b shows the main vortical structures found in the flow.

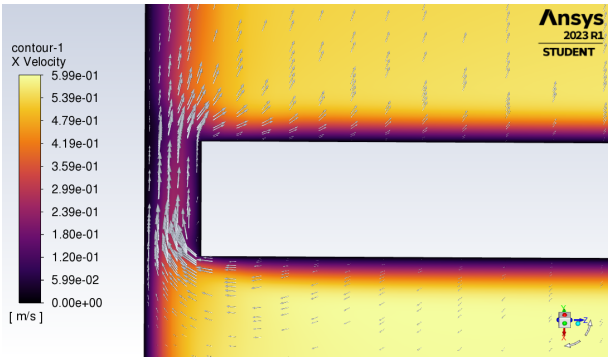

(a) Velocity vector field at plane tangent to the camber line at $x/c_a x = 0.4$, coloured with u velocity component

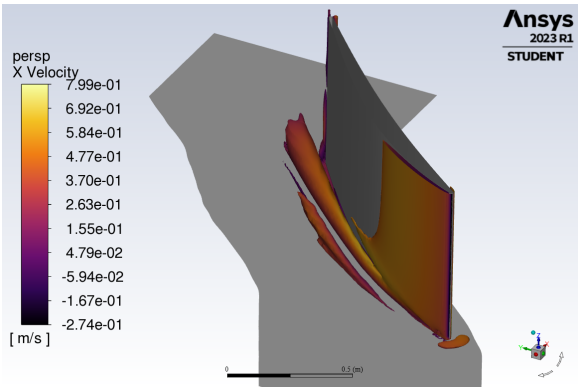

(b) Vortex Identification for $\lambda_2 = -5$

Figure 4.1: Velocity Vector Field and $\lambda_2 = -5$ Isosurface

The vortical structures will be detected using the λ_2 vortex identification criterion. This algorithm is based on the analysis of the velocity gradient tensor. The first step is defining the velocity gradient tensor:

$$\nabla \mathbf{V} = \begin{bmatrix} \frac{\partial u}{\partial x} & \frac{\partial u}{\partial y} & \frac{\partial u}{\partial z} \\ \frac{\partial v}{\partial x} & \frac{\partial v}{\partial y} & \frac{\partial v}{\partial z} \\ \frac{\partial w}{\partial x} & \frac{\partial w}{\partial y} & \frac{\partial w}{\partial z} \end{bmatrix} \tag{4.1}$$

Then, the symmetric part of the velocity gradient tensor S is calculated:

$$\mathbf{S} = \frac{1}{2}(\nabla \mathbf{V} + (\nabla \mathbf{V})^T) \tag{4.2}$$

Next, the antisymmetric part of the velocity tensor is calculated:

$$\mathbf{W} = \frac{1}{2}(\nabla \mathbf{V} - (\nabla \mathbf{V})^T) \tag{4.3}$$

The $S^2 + W^2$ term's eigenvalues are considered to determine the existence of local pressure minimums due to vortical motion. Vortex core regions will present two negative eigenvalues. If λ_1, λ_2, λ_3 are the eigenvalues, and $\lambda_1 \geq \lambda_2 \geq \lambda_3$, vortex cores can be found as interconnected regions for negative values of the λ_2 eigenvalue. This explanation has been taken from [23], see the paper for detailed information. To represent the vortical structures, iso-surfaces will be created for fixed values of λ_2.

In the three-dimensional simulations, the total pressure loss coefficient will be used to characterize the energy losses. Unlike the two dimensional simulations that yielded a single value, this time a curve representing the variation of the total pressure loss along the z direction planes will be plotted for each simulation. This allows for a more detailed analysis of the pressure losses throughout the computational domain. Figure 4.2 shows the curve obtained for the default GEKO coefficient's setup and the reference data.

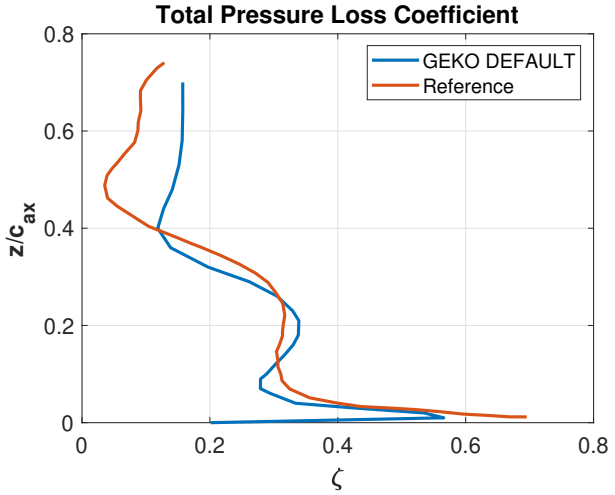

Figure 4.2: Total Pressure Loss Coefficient along the z Direction

4.2 3D Meshing and Boundary Conditions

The different blocks of the two dimensional mesh were extruded in the z direction in order to generate the three dimensional mesh. The first approach consisted on extruding all the already existent blocks for a height of $z/c_{ax} = 0.7$, and extruding the remaining airfoil region of the gap (highlighted in green in figure 4.3a) for a height of $s/c_{ax} = 4.39\%$ to match the gap height. However, this approach proved to be challenging as connecting the meshes of the extruded blocks with the airfoil gap region was complex. Ensuring the same number of elements and spacing in the z-direction for both the extruded blocks and the airfoil's gap region required manually setting the distribution of points through edge sizings. Despite the apparent interconnectedness of the mesh, running simulations resulted in incoherent results due to improper mesh node connections. Figure 4.3 illustrates the geometry of the first approach.

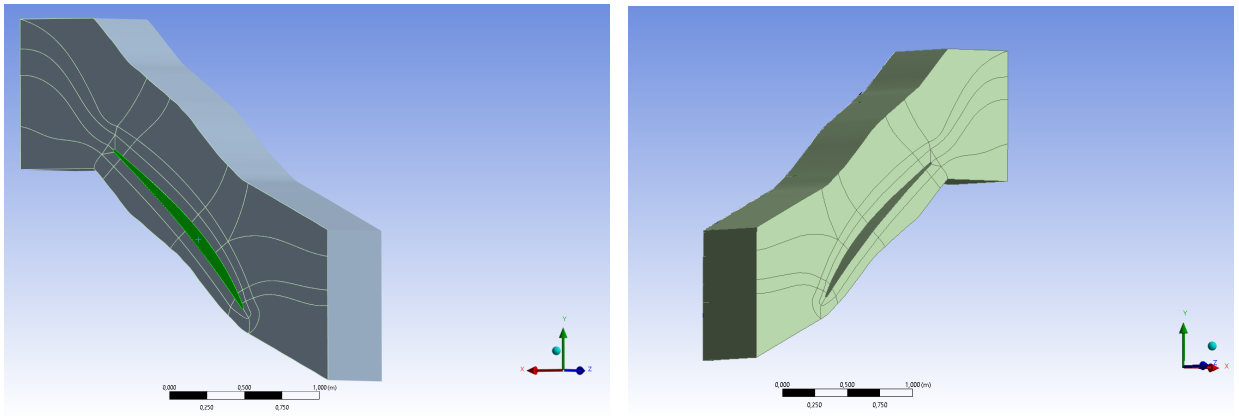

(a) First Approach Geometry. Endwall Side View.

(b) First Approach Geometry. Front View

Figure 4.3: First Approach Geometry

The second approach consisted on first extruding the entire gap region as a single block for the gap's height, and then extruding the entire domain without the airfoil region for the remaining height. To divide the domain into different blocks, the edges of the two-dimensional mesh were projected onto both the frontal and back planes. Unlike the first approach, this time the mesh was fully connected. However, the meshing software did not maintain all the edges in the z direction parallel to each other, see figure 4.4a. This was a very critical issue, because without parallel z direction edges, the airfoil shape could not be preserved properly. Figure 4.4b illustrates the deformation of the blade's shape caused by the sweeping of the z direction edges along the leading edge. In this mesh configuration, the airfoil region of the gap had also been structered. Nevertheless, the quality of the elements was significantly compromised due to the high skewness of the cells.

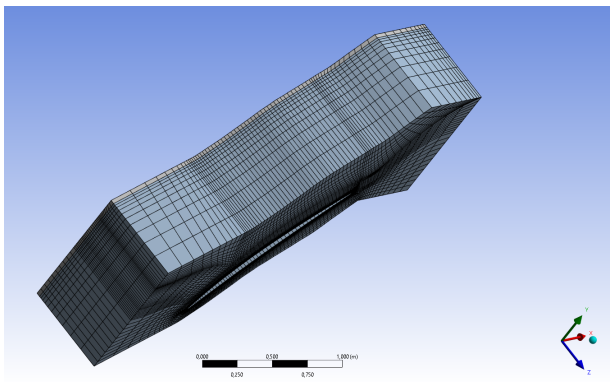

(a) Edges in z Direction

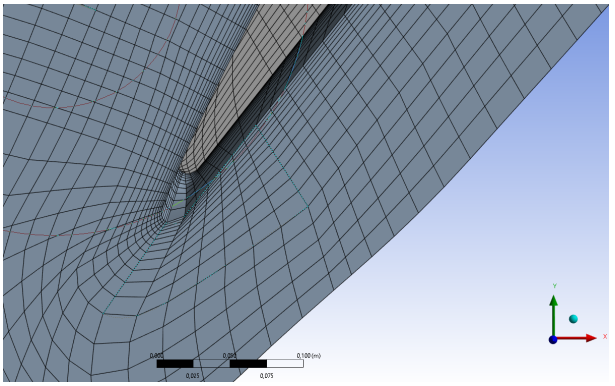

(b) Second Approach Mesh

Figure 4.4: Second Approach Mesh

The third approach consisted on individually extruding each meshing block for the gap height, including the airfoil section. Subsequently, all the sections, excluding the airfoil region, were extruded again for the remaining height. This was the most time consuming approach, since a total of 72 blocks were extruded, and each edge of the blocks had to be manually sized. However, it ensured the proper connection of the gap region nodes. Figure 4.5 illustrates the blocks of the geometry. Meshing the blade region of the gap presented the greatest challenge, specially at the leading and trailing edges. The first approach to mesh this region involved completely structuring the entire region. Good quality elements were obtained in the middle section of the blade, but very high skewness elements were obtained at the leading and trailing edges; see figure 4.6.

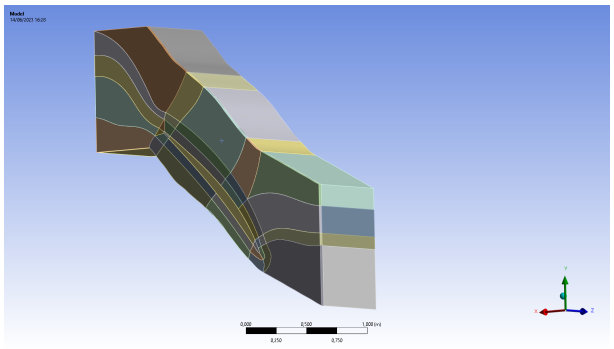

(a) Edges in z direction

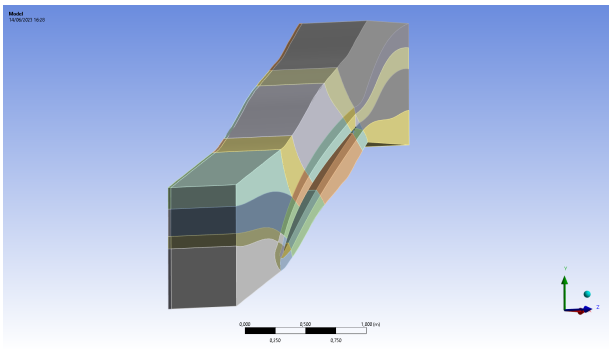

(b) Second Approach Mesh

Figure 4.5: Third Approach Mesh

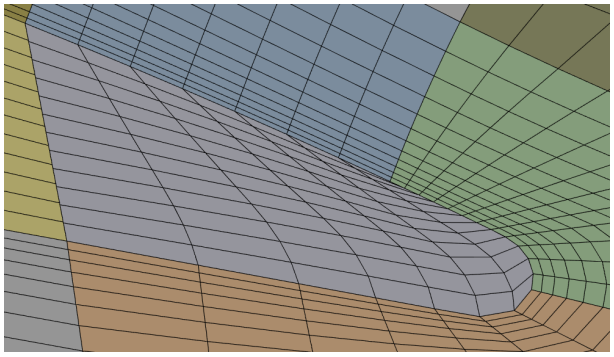

(a) Leading Edge Gap Region

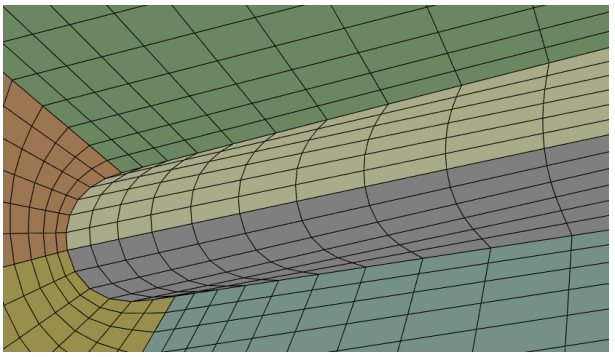

(b) Trailing Edge Gap Region

Figure 4.6: Leading and Trailing Edges Gap Region Structured Mesh

An unstructured mesh approach was also attempted for these problematic regions, but due to the different sizings of the surrounding elements, the results obtained for this approach were also unsatisfactory. At last, a hybrid meshing strategy was applied for this region. Structured inflation layers were added to prevent large size jumps between the surrounding elements and this region's elements, while the mesh in the inner region remained unstructured; see figure 4.7. Note that the mesh illustrated in figure 4.7 is finer than the previous ones, since these images were taken from the final mesh. This hybrid strategy yielded better results than the previous approaches, although some low quality elements were still present in the mesh. To properly structure these regions, the base geometry for constructing the blocks would have to be modified, and at this stage of the project there was not enough time to do that, so the simulations were run using this mesh configuration.

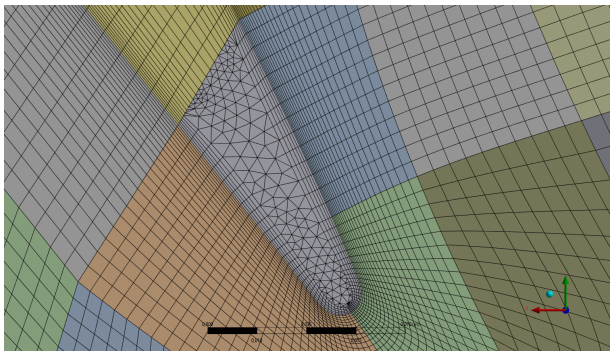

(a) Leading Edge Gap Region

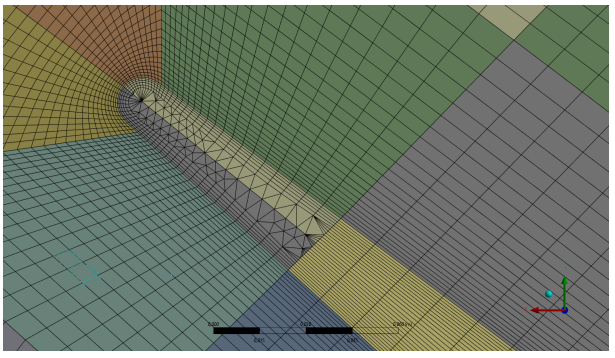

(b) Trailing Edge Gap Region

Figure 4.7: Leading and Trailing Edges Gap Region Hybrid Mesh

The final mesh was generated by applying the same edge sizings used in the 2D base mesh, as it stroke a balance between accuracy and the total number of elements. The number of mesh planes in the z direction was limited by the Ansys Students License, which allowed a maximum of 512.000 elements. Consequently, a thorough mesh convergence study in the z direction could not be conducted. For the gap region, six mesh planes were employed, and 22 mesh planes were utilized for the remaining region. See the planes distribution in figure 4.8a. Although this may initially appear as a coarse mesh for the case, it will be demonstrated in the next sections that the obtained results were satisfactory. Figure 4.8 illustrates the final three dimensional mesh.

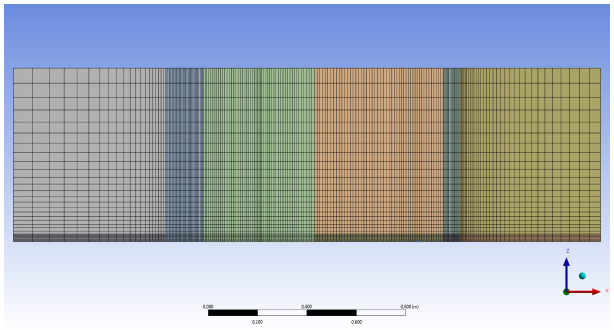

(a) Bottom View

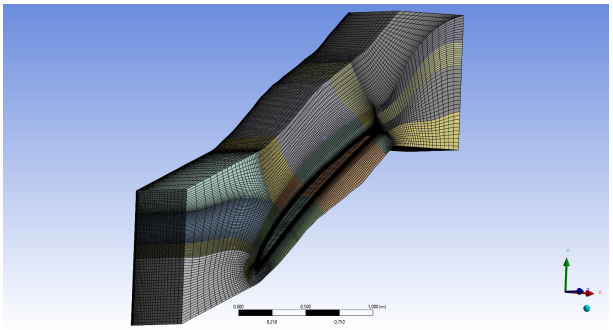

(b) 3D view

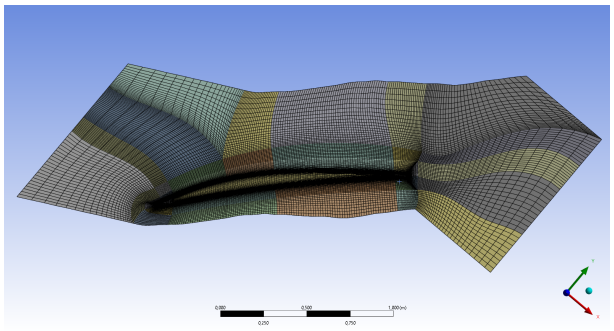

(c) Rotated Front View

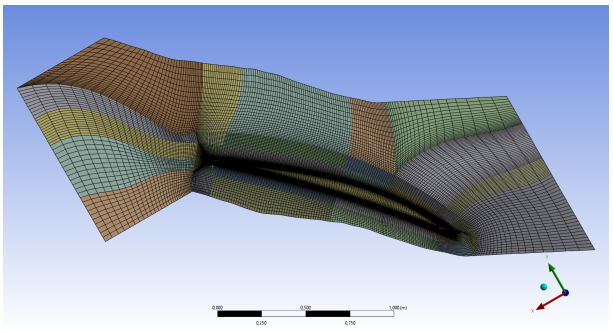

(d) Rotated Back View

Figure 4.8: Final 3D Mesh

The three dimensional case introduces three new walls: the blade tip wall, the front wall, and the back wall (endwall). Non-slip wall boundary conditions will be applied to the endwall and the blade tip wall. On the other hand, symmetry boundary conditions will be set for the front wall. The symmetric boundary condition, applied to a specified wall, assumes that the flow exhibits symmetry, resulting in no flow across the boundary. This reduces the computational cost, as calculations need to be performed only for a portion of the domain. The rest of the boundary conditions will remain the same as in the 2D case (inlet, outlet, bottom, and top). The inflow velocity components will change respect to the 2D simulations, since those values accounted for correction factors that will not be needed in this case. The inflow velocity for this case will have an angle of $60.75deg$ with respect to the horizontal axis. The turbulent intensity at the inlet will remain the same (1%), and the turbulent length scale will be set to $10^{-3}m$, since this was the value that provided results that closely matched the reference data in the inlet boundary conditions study.

4.3 Total Pressure Loss Coefficient

The results for the 3D simulations will be assessed mainly by the Total Pressure Loss Coefficient. From the results depicted in figure 4.9, it can be argued that the RANS simulations achieve to capture the overall pressure loss tendencies along the z direction, despite not perfectly matching the reference data. It should be noted that the reference simulation from [20] was conducted with variable inlet velocity fluctuations, whereas the simulations run in the present study used a fixed value for the entire inlet. In the reference paper, the fluctuations near the endwall were an order of magnitude higher than the ones at the mid-span.

The standard $k-\omega$ simulation exhibits a tendency to overestimate the pressure losses, this is a clear sign of the intrinsic dissipative behaviour of the RANS formulation. For the region near the endwall, the $k-\omega$ simulation matches the reference values, while the GEKO default falls short. Based on the observed behaviour of the different simulations, it can be suggested that if the same turbulent boundary conditions of the Reference simulations were applied to the RANS simulations, the $k-\omega$ model would have overestimated the pressure losses in the gap region. On the other hand the GEKO model predicts lower pressure losses in the near endwall region, although it is expected that the pressure losses would increase if the Reference turbulent boundary conditions were applied.

For the rest of the domain, the GEKO model yields results closer to the reference values by estimating lower pressure loss coefficients. The higher dissipation for $z/c_{ax} > 0.4$ can be attributed to various factors: the influence of the symmetry boundary condition, the intrinsic RANS modelling averaging, and the lack of mesh resolution in that region. Regarding the different GEKO configurations, even though the CJET parameter appeared to improve the results in the 2D simulations, in the three dimensional case, its effects are almost negligible. Considering that the reference simulation used 60 million elements, while the RANS simulations only use around 500 thousand elements, the results achieved by the GEKO model are deemed satisfactory.

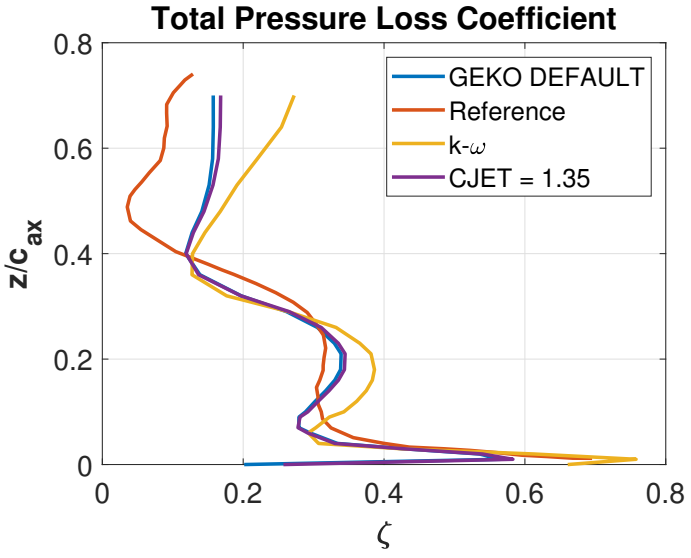

Figure 4.9: Total Pressure Loss Coefficient along z Direction

4.4 Pressure and Skin Friction Coefficients

The distribution of pressure and friction coefficients along the z direction is illustrated in Figure 4.10. To avoid overcrowding and maintain clarity in the data visualization, the reference data is not included in the plots. However, the author has compared the results and observed similar trends. In terms of the pressure coefficient, the plots may deviate from the reference data due to a disparity in the reference pressure value used to calculate this coefficient. As the z value increases, the pressure coefficient tends to increase on the pressure side and decrease on the suction side. Consequently, this leads to a higher lift coefficient at the root of the blade. This phenomenon arises from the absence of vortices in that specific region. Additionally, the friction coefficient exhibits an increase near the gap on both the pressure and suction sides. This observation demonstrates how vortical structures enhance energy dissipation by elevating friction.

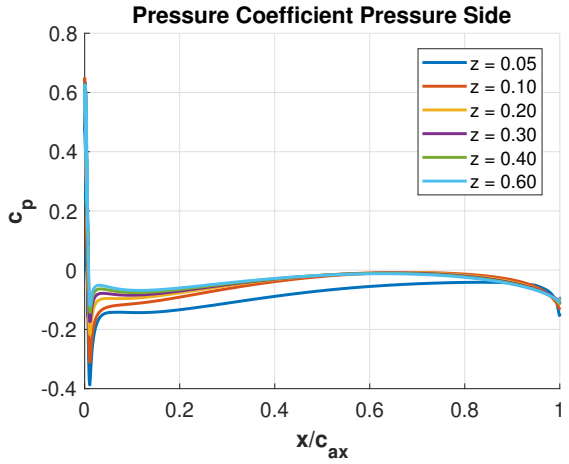

(a) c_p PS

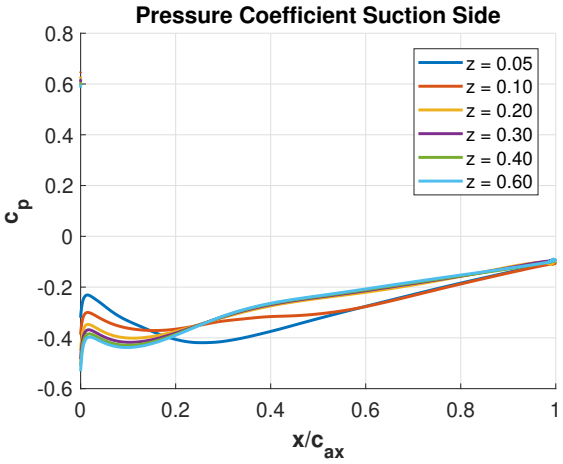

(b) c_p SS

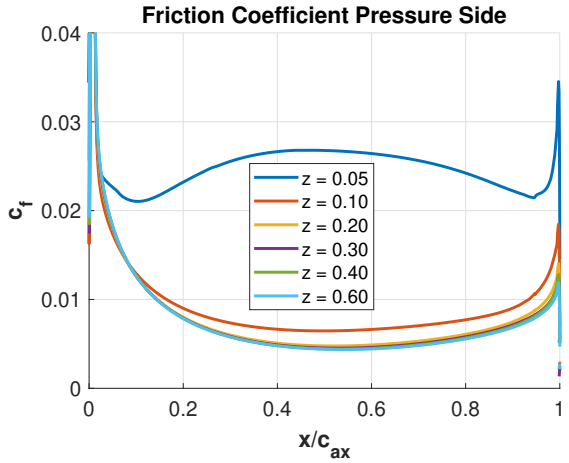

(c) c_f PS

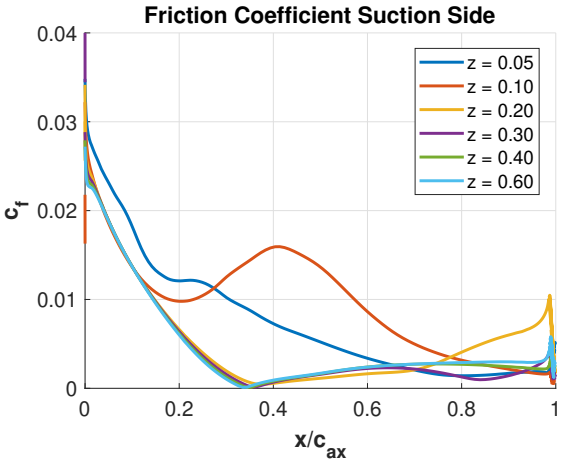

(d) c_f SS

Figure 4.10: Pressure and Friction Coefficients along the xy Planes along Different z values.

4.5 Vortex Structures Analysis

As explained in the flow description section. the main vortical structures on the flow are identified through the λ_2 vortex identification criterion. Figure 4.11 illustrates λ_2 isosurfaces coloured with the u velocity component. The Tip Leakage Vortex is easily identified as the major vortical structure. Parallel to this structure, two more induced vortices are detected in the reference data. However, only one of the induced vortices is detected in the RANS simulations. A horse-shoe vortex is also detected near the endwall region of the leading edge. Additionally, a structure is detected at the front part of the suction surface. This structure is not a vortex; the identification criterion is detecting the flow acceleration across this surface as a vortex. In the reference simulation, a large set of smaller vortices are detected towards the trailing edge of the blade. These structures are result of a separation bubble. However, the presence of these smaller vortices is reduced in the RANS simulations due to the absence of the separation bubble.

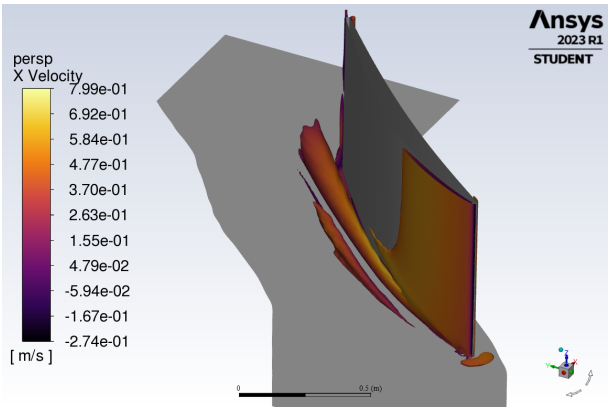

(a) GEKO Default. $\lambda_2 = -5$

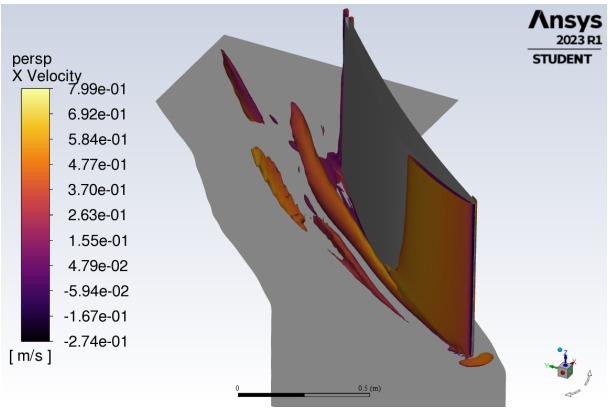

(b) $K - \omega$. $\lambda_2 = -8$

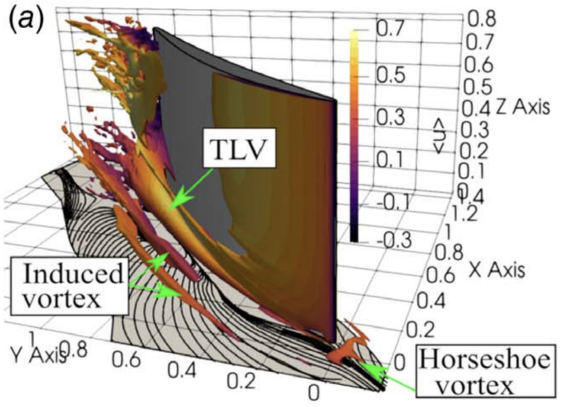

(c) Reference. $\lambda_2 = -3$

Figure 4.11: Vortical Structures Isosurfaces

Different values of λ_2 have been tested for each simulation to detect vortical structures. Through experimentation, it was determined that a value of $\lambda_2 = -5$ for the GEKO simulation, and the value of $\lambda_2 = -10$ for the $k - \omega$ simulation provided contours that closely resembled the reference data. In comparison to the $k - \omega$, the GEKO simulation exhibited vortical shapes that closely matched the reference data for the tip leakage and induced vortices. However, the $k - \omega$ presents additional disturbances in the flow above the aforementioned vortices that do not correspond to coherent vortex structures.

Figures 4.12, 4.13, 4.14 and 4.15 present the vortices identified using the λ_2 criterion (highlighted in red) and the Q criterion (highlighted in green) along planes that are tangent to the camber line. These planes are also coloured based on the magnitude of vorticity. It is worth noting that the perspectives of the simulation images vary due to the limitation of Ansys tools, which do not allow for direct positioning of the camera in a perpendicular and orthogonal view with respect to the planes. See more information about the Q criterion in [24] and [25].

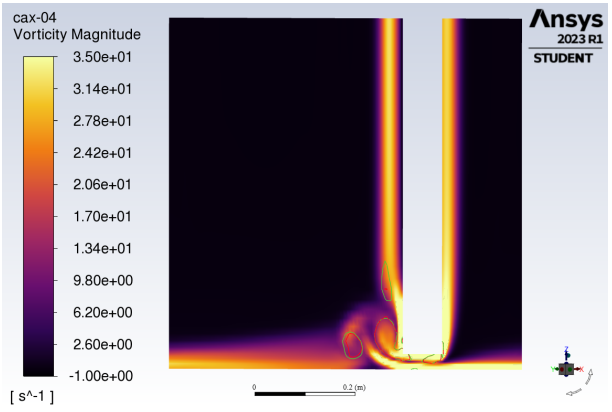

(a) GEKO Default. $Q = 10$, $\lambda_2 = -5$

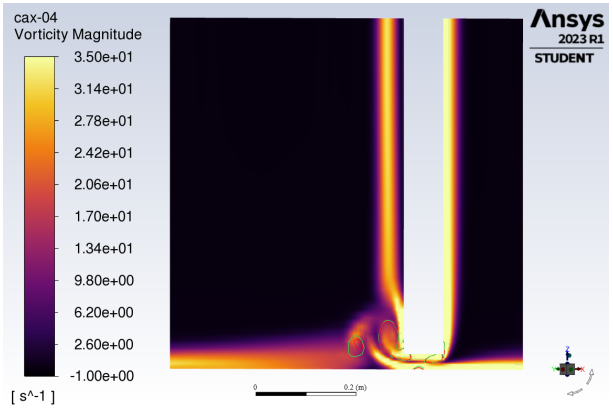

(b) $k - \omega$. $Q = 10$, $\lambda_2 = -10$

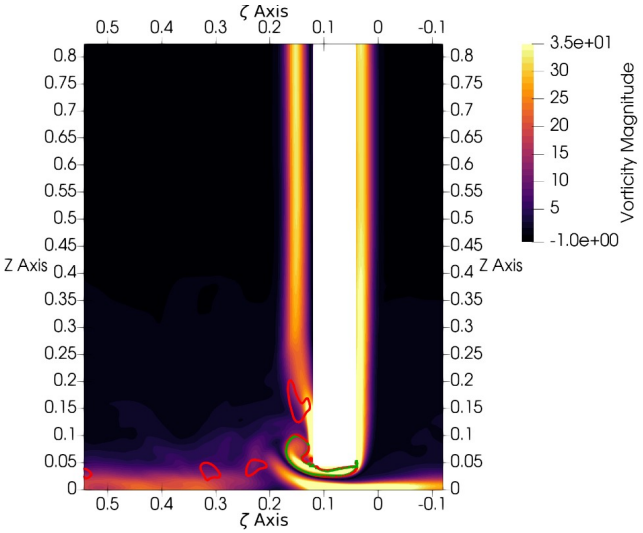

(c) Reference. $Q = 10$, $\lambda_2 = -3$ [26]

Figure 4.12: Vortical Structures at $x/cax = 0.4$

The obvious difference between the RANS and the Reference simulations lies in the image resolution and the level of detail, primarily due to the finer mesh employed in the LES simulation of the reference. The RANS simulations also exhibit smoother contours, which can be attributed to the temporal and spatial averaging inherent in the equations. For the tangent to the camberline planes at $x/c_{ax} = 0.4$ and $x/c_{ax} = 0.6$, the vorticity intensity of the boundary layer is quite similar across all cases. The tip leakage vortex is detected in all three cases with both the λ_2 and Q criterion. Its position and size are also similar across all three methods, however, the RANS similations predict a higher vorticity intensity at the outer-left part of the diameter of the vortex. Only one of the induced vortices are detected with these vortex identification methods in the RANS simulations. The positioning of the induced vortex is similar in all three simulations, but the shape differs between the RANS and Reference simulations. In the GEKO simulation, an additional vortex at the suction surface is detected as in the Reference simulation, see figure 4.12a. Finally, the vorticity intensity of the endwall boundary layer also seems to be higher in the RANS simulations for the $x/c_{ax} = 0.4$ plane.

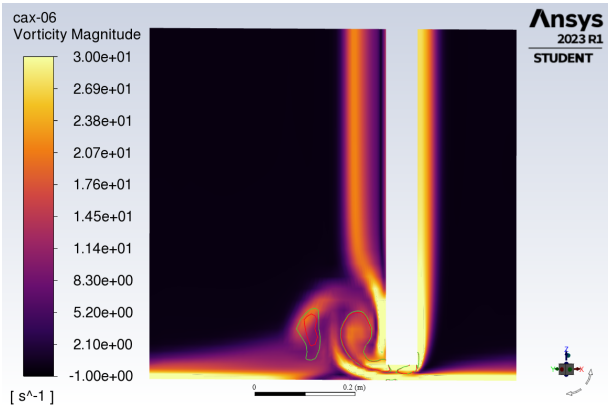

(a) GEKO Default. $Q = 10$, $\lambda_2 = -5$

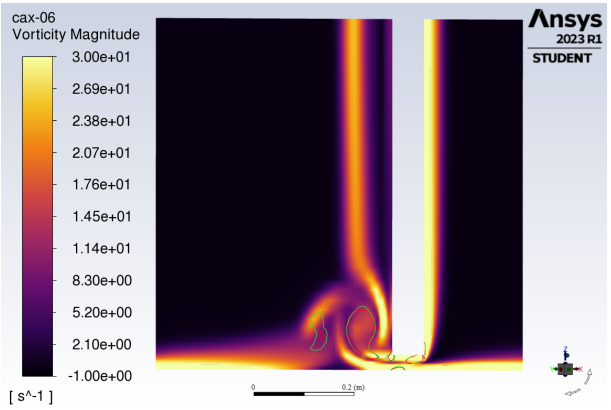

(b) $k - \omega$. $Q = 10$, $\lambda_2 = -10$

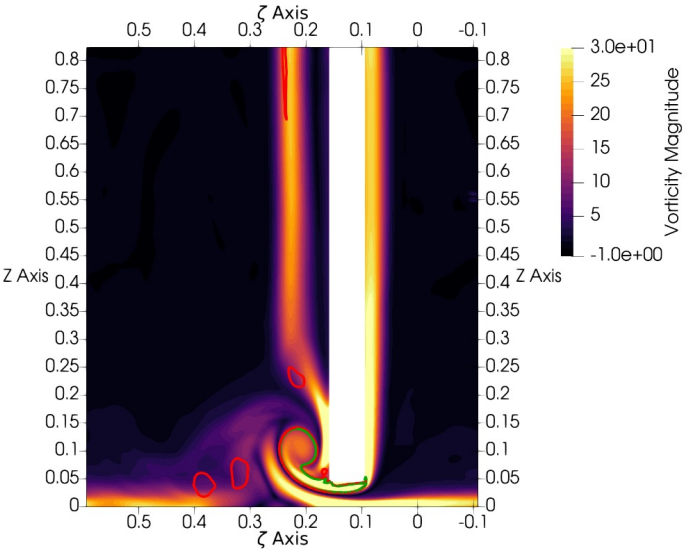

(c) Reference. $Q = 10$, $\lambda_2 = -3$ [26]

Figure 4.13: Vortical Structures at $x/cax = 0.6$

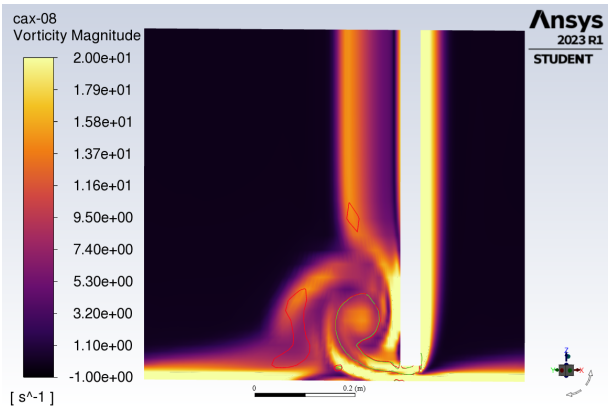

(a) GEKO Default. $Q = 10$, $\lambda_2 = -5$

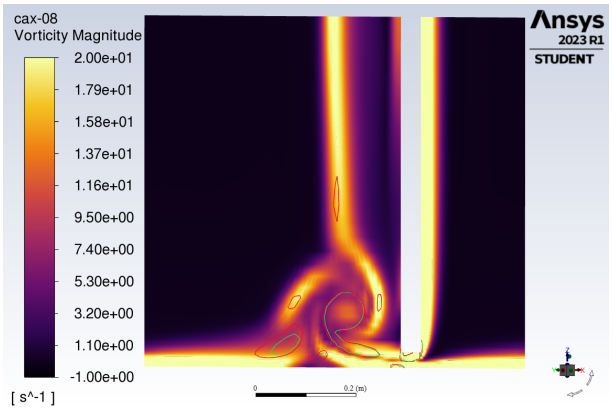

(b) $k - \omega$. $Q = 10$, $\lambda_2 = -10$

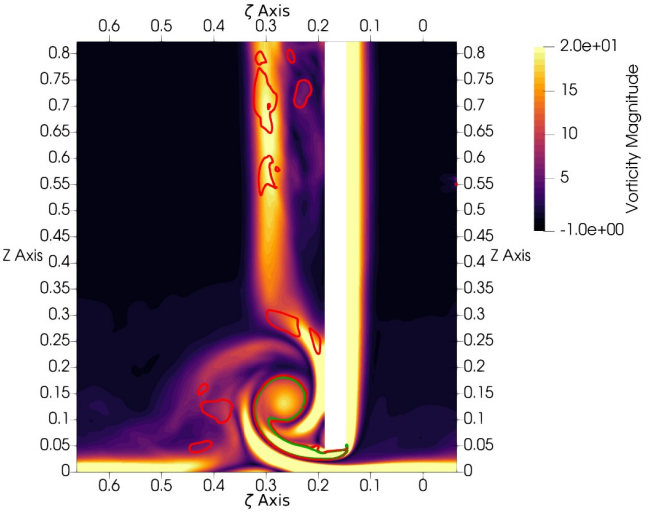

(c) Reference. $Q = 10$, $\lambda_2 = -3$ [26]

Figure 4.14: Vortical Structures at $x/cax = 0.8$

For the tangent to the camberline plane at $x/c_{ax} = 0.8$, the position of the tip leakage vortex is similar in the Reference and GEKO simulations. Although the size of the vortex in all three cases is similar, the vortex is not in contact with the suction surface in the $k - \omega$ simulation. Smaller vortical structures caused by the separation bubble are detected in the Reference simulation, but they are not present in the RANS plots for neither vortex detection criterion. At last, in the GEKO simulation, the separation layer at the suction side is thicker but less intense than the ones found in the $k - \omega$ and Reference simulations.

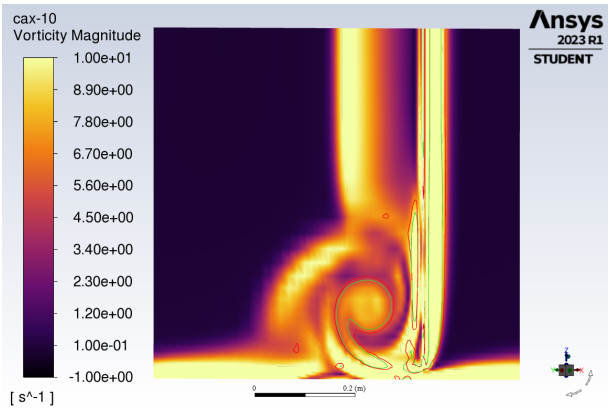

(a) GEKO Default. $Q = 10$, $\lambda_2 = -5$

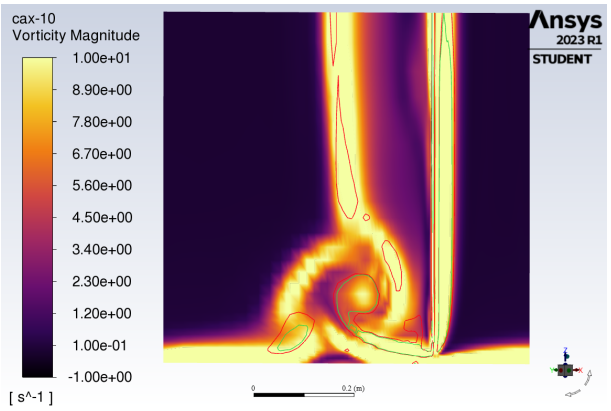

(b) $k - \omega$. $Q = 10$, $\lambda_2 = -10$

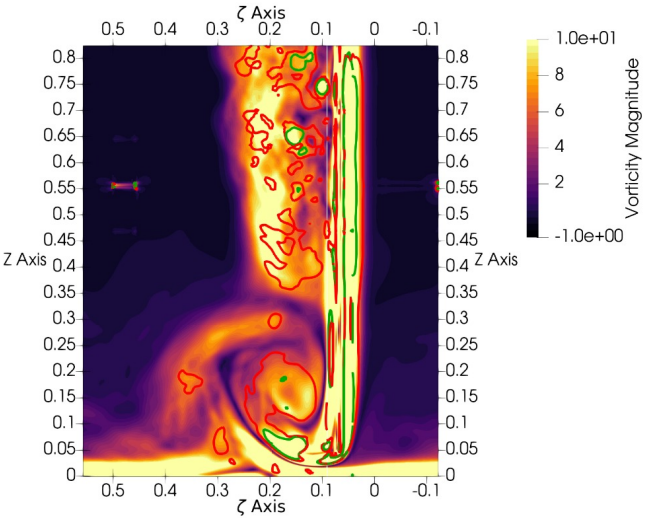

(c) Reference. $Q = 10$, $\lambda_2 = -3$ [26]

Figure 4.15: Vortical Structures at $x/cax = 1$

Lastly, in the tangent to the camberline plane located at $x/c_{ax} = 1$, the tip leakage vortex is once again observed to be separated from the suction surface in the $k - \omega$ simulation, and the intensity of the vortex is slightly overestimated in the RANS simulations. The reference figure depicts the smaller vortical structures found at the suction side of the trailing edge, while no vortical structures are found in that region in the GEKO simulation. The $k - \omega$ detects a large structure in the mentioned region, but this result is not accurate according to the Reference illustration.

In conclusion, the main vortical structure, the tip leakage vortex, has been found in all three simulations. Its positioning is almost identical until $x/c_{ax} = 0.6$ across all different simulations. From that point, the $k - \omega$ model predicts a separation of the vortex from the suction surface, while in the Reference and GEKO simulations the vortex remains in contact with the surface. The outer part of the vortices are predicted with a higher intensity in all three cases. The boundary layers along the walls are slightly thicker in the RANS simulations. These two observations are product of the intrinsic dissipative behaviour of the RANS formulation aforementioned.

Chapter 5

Concluding Remarks

5.1 Study Conclusions

The objective of this thesis was to conduct a thorough examination of the suitability of the Ansys GEKO turbulence model for analyzing fluid flow in a turbomachinery compressor cascade. This thesis serves as a first step towards a fully calibrated model for the study case. Initially, two dimensional simulations were performed by simulating the compressor's blade's mid-span. These simulations required generating a two dimensional mesh and studying its convergence. This involved building multiple meshes with different levels of refinement.

The entire project was subject to a software limitation imposed by the Ansys Student's License, which imposed a maximum limit on the number of mesh elements. The mesh selection was constrained due to this limitation. The chosen mesh had to consider its future extrusion to generate the three dimensional mesh, and ensure sufficient resolution in the extruded direction to effectively capture intricate flow phenomena.

After selecting a mesh that achieved a balance between the number of elements and converged results, the impact of turbulent boundary conditions was evaluated. As explained in the introduction, the employed turbulence model is a variation of the standard $k-\omega$ model, and several studies have consistently demonstrated that it exhibits a high degree of sensitivity to the inlet boundary conditions[16]. Different inlet boundary conditions based on [21] were examined. The selection criteria involved matching the total pressure loss values at the mid-span provided by [22].

Subsequently, a first approach towards the calibration of the model was taken by using the selected two dimensional mesh, and examining the sensitivity of the different free parameters of the GEKO model. All the parameters were modified individually to understand their influence in the study flow. After conducting the sensitivity assessment, it was found that most influential parameter was the CSEP coefficient. The only parameter that enhanced simulation results was the CJET parameter. The decision to conduct this study using a two-dimensional mesh was driven by the need to perform a large number of simulations to assess parameter behaviour. Time constraints made it impractical to carry out such investigations in a

three-dimensional case.

Once the GEKO model was calibrated for the two dimensional case, the resulting free parameters were employed to conduct three dimensional simulations. The three dimensional mesh creation was the most time consuming part of the study, and due to the author's inexperience, the generated mesh was not optimal. A significant number of elements were allocated for each mesh plane of the three-dimensional mesh, resulting in a lower resolution in the extruded direction compared to the plane's resolution. This limitation arose as the maximum number of allowed elements had already been reached. Due to the lack of available mesh elements, an exhaustive mesh convergence study in the extruded direction could not be conducted.

For the three-dimensional case, three simulations were conducted: one utilizing the default GEKO parameters, another employing the calibrated GEKO model, and a third employing the standard $k-\omega$ model. Despite the relatively lower resolution of the mesh in the extruded direction, all three simulations successfully captured comparable trends in the pressure loss coefficient along the span-wise direction, similar to the reference data from [20]. However, none of the simulations achieved to precisely capture exact values. It should be noted that the reference data originated from a Large Eddy Simulation (LES) employing 60 million elements, thus, this discrepancies were already expected. The $k-\omega$ model tended to overestimate pressure losses, while the GEKO models yielded values closer to the Reference. There were no significant differences between the calibrated and default GEKO models, both models produced similar outcomes.

Moreover, the vortical structures of the flow were identified using the λ_2 and Q criterion, and compared with data from [26]. The tip leakage and horse-shoe vortices were detected by both RANS models. However, in these simulations, only one of the induced vortices were detected. Further, the smaller vortices produced by the separation bubble in the Reference simulation, were not detected by the RANS simulations. The GEKO simulation accurately predicted the size and location of the tip leakage vortex, while the standard $k-\omega$ model failed to precisely predict its location for values of $x/c_{ax} > 0.6$.

Throughout this study, it has been made evident that the GEKO model enhances the performance of the standard $k-\omega$ model. Considering that only half a million mesh elements were utilized, compared to the 60 million elements employed in the reference LES simulation, the obtained results are deemed satisfactory. However, from this study alone, it is hard to justify the price of the Ansys software solution. Further investigation with local calibration of the parameters would be required to optimize the model calibration for the case, and determine if the obtained results justify the expense. Nevertheless, this general study has showcased the potential of the GEKO model.

5.2 Future Research

Despite conducting a general study of the GEKO model for the present case, numerous areas of investigation have remained unexplored due to time constraints. It is crucial to highlight several key areas that warrant further exploration in future research:

- **1. Mesh Optimization:** Having gained experience in generating three-dimensional meshes, the author now possesses the knowledge to properly structure the gap region mesh, particularly at the blade region. Furthermore, considering the limitation on the number of mesh elements, additional studies on mesh optimization would be necessary to refine critical areas by reallocating elements. Lastly, implementing a symmetric meshing approach in the periodic zones would eliminate interpolation errors and improve overall accuracy.
- **2. Inlet Boundary Condition:** As mentioned throughout the study, the turbulent fluctuations at the inlet were maintained constant. However, in future research, it would be valuable to incorporate variable inlet conditions as outlined in the reference paper [20] by utilizing user-defined functions. This would enable a more comprehensive exploration of the impact of varying inlet conditions on the flow behaviour.
- **3. Parameter Tuning in 3D Simulations:** In this study, the modification of GEKO coefficients was limited to two-dimensional simulations. However, it would be valuable to investigate the effects of modifying all parameters again specifically for the three-dimensional case. Additionally, Ansys offers the capability of locally tuning the parameters through scripting, which presents numerous opportunities for further research and exploration.
- **4. Higher Re Simulations:** In this study, simulations were conducted at a relatively low Reynolds number. However, it would be valuable to investigate the behavior of different GEKO parameters at higher Reynolds numbers and assess if the model continues to yield accurate results. Exploring the model's performance in such conditions would provide insights into its applicability across a wider range of turbomachinery cases.

Chapter 6

Environmental Impact

6.1 Implications

Gas turbines have a notable environmental impact as they rely on the consumption of hydrocarbon fuels. This consumption leads to the release of greenhouse gases, particularly carbon dioxide, contributing to climate change. Enhancing the efficiency of turbomachinery is key to address this issue. Further, this study focuses on investigating the potential of using a calibrated GEKO turbulence model to obtain prompt results for turbomachinery preliminary design. This approach offers substantial energy savings, as Large Eddy Simulations, such as the reference paper simulation [20], are significantly more computationally demanding than RANS simulations. It is true that RANS simulations do not provide enough accuracy for final development stages. Nevertheless, they can serve as an initial approach to assess new conceptual designs and explore innovative alternatives more efficiently.

6.2 Environmental Footprint

In this study, the primary source of CO2 emissions stems from the computer used to conduct simulations and present results, which had a power supply of 750W. Although the computer was not consistently operating at full power throughout the entire duration of the study, it remained active, performing simulations even when the student was not directly engaged in thesis work. Thus, to estimate the environmental impact, it is considered that the computer consumed 750W for the entire project duration. Additionally, the energy consumption of the workspace lighting needs to be taken into account. A LED light bulb with a power consumption of 25W was used for illumination, and the total number of study hours will be factored into the overall light consumption calculation. The specific CO2 emission factor has been taken from the author's electricity bill information. Table 6.1 reflects the environmental footprint of this thesis.

Source	**Time (h)**	**Power (kW)**	**Energy (kWh)**	**Specific Emissions (kg CO2/kWh)**	**Total Emissions (kg CO2)**
Computer	600	0.75	450	0.204	91.8
Lighting	600	0.025	15	0.204	3.06
Total					94.86

Table 6.1: Carbon Footprint

References

[1] J. D. Denton. "The 1993 IGTI scholar lecture: Loss mechanisms in turbomachines". In: *Journal of Turbomachinery* 115.4 (1993), pp. 621–656. DOI: 10.1115/1.2929299.

[2] A N Kolmogorov. "Local structure of turbulence in an incompressible viscous fluid at very high Reynolds Numbers". In: *Soviet Physics Uspekhi* 10.6 (1968), pp. 734–746. DOI: 10.1070/pu1968v010n06abeh003710.

[3] V. P. Maslov. "Kolmogorov law and Kolmogorov and Taylor scales in anisotropic turbulence. turbulence as a result of three-scale interaction". In: *Theoretical and Mathematical Physics* 94.3 (1993), pp. 260–264. DOI: 10.1007/bf01017256.

[4] Steven B. Pope. *Turbulent flows*. Cambridge University Press, 2000.

[5] Toshiyuki Gotoh. "Energy spectrum in the inertial and dissipation ranges of two-dimensional steady turbulence". In: *Physical Review E* 57.3 (1998), pp. 2984–2991. DOI: 10.1103/physreve.57.2984.

[6] Charles Hirsch. *Numerical computation of internal and external flows*. Elsevier/Butterworth-Heinemann, 2007.

[7] Bernard Geurts. *Elements of direct and large-eddy simulation*. R.T. Edwards, 2004.

[8] Uriel Frisch. *Turbulence: The legacy of A.N. Kolmogorov*. Cambridge Univ. Press, 2009.

[9] Michael A. Leschziner. "Reynolds-averaged navier-stokes methods". In: *Encyclopedia of Aerospace Engineering* (2010). DOI: 10.1002/9780470686652.eae054.

[10] François G. Schmitt. "About Boussinesq's turbulent viscosity hypothesis: Historical remarks and a direct evaluation of its validity". In: *Comptes Rendus Mécanique* 335.9–10 (2007), pp. 617–627. DOI: 10.1016/j.crme.2007.08.004.

[11] B.E. Launder and B.I. Sharma. "Application of the energy-dissipation model of turbulence to the calculation of flow near a spinning disc". In: *Letters in Heat and Mass Transfer* 1.2 (1974), pp. 131–137. DOI: 10.1016/0094-4548(74)90150-7.

[12] Lars Davidson. In: *An Introduction to Turbulence Models* (Feb. 1997). URL: https://www.tfd.chalmers.se/~lada/postscript_files/kompendium_turb.pdf.

[13] W.P Jones and B.E Launder. "The prediction of laminarization with a two-equation model of turbulence". In: *International Journal of Heat and Mass Transfer* 15.2 (1972), pp. 301–314. DOI: 10.1016/0017-9310(72)90076-2.

[14] David Wilcox. "4.4. CLOSURE COEFFICIENTS". In: *Turbulence modeling*. DCW Industries, 2006, pp. 135–138.

[15] David C. Wilcox. *Turbulence modeling*. DCW Industries, 2006.

[16] F. R. Menter. "Influence of freestream values on K-Omega Turbulence model predictions". In: *AIAA Journal* 30.6 (1992), pp. 1657–1659. DOI: 10.2514/3.11115.

[17] Johan C. Kok. "Resolving the dependence on freestream values for the K-Omega Turbulence model". In: *AIAA Journal* 38 (2000), pp. 1292–1295. DOI: 10.2514/3.14547.

[18] R. Lechner F.R. Menter. "Best Practice: Generalized $k-\omega$ Two-Equation Turbulence Model in ANSYS CFD (GEKO)". In: *ANSYS German GmbH* (2019).

[19] Jordi Ventosa Molina. "Compressors and Turbines". In: *CENTRE TECNOLÒGIC DE TRANSFERÈNCIA DE CALOR (CTTC), ESEIAAT Lectures* (2016).

[20] Jordi Ventosa-Molina et al. "Study of relative endwall motion effects in a compressor cascade through direct numerical simulations". In: *Journal of Turbomachinery* 143.1 (2020). DOI: 10.1115/1.4049101.

[21] Peter Busse et al. "Effects of turbulent boundary conditions on the prediction of the secondary flow field in a linear compressor cascade". In: *Volume 2A: Turbomachinery* (2016). DOI: 10.1115/gt2016-56455.

[22] David Engelmann et al. "Near-wall flow in turbomachinery cascades—results of a German collaborative project". In: *International Journal of Turbomachinery, Propulsion and Power* 6.2 (2021), p. 9. DOI: 10.3390/ijtpp6020009.

[23] Jinhee Jeong and Fazle Hussain. "On the identification of a Vortex". In: *Journal of Fluid Mechanics* 285 (1995), pp. 69–94. DOI: 10.1017/s0022112095000462.

[24] Václav Kolář. "Vortex identification: New requirements and limitations". In: *International Journal of Heat and Fluid Flow* 28.4 (2007), pp. 638–652. DOI: 10.1016/j.ijheatfluidflow.2007.03.004.

[25] Yves Dubief † and Franck Delcayre ‡. "On coherent-vortex identification in turbulence". In: *Journal of Turbulence* 1 (2000). DOI: 10.1088/1468-5248/1/1/011.

[26] Alexandre Juanico Sala. "Study on Vortex Visualisation Techniques for Turbomachinery Flows". In: *ESEIAAT TFG (Private Communication)* (2023).